Materials Today Bio 28 (2024) 101244

Contents lists available at ScienceDirect

Materials Today Bio

journal homepage: www.journals.elsevier.com/materials-today-bio

# Delivery of extracellular vesicles loaded with immune checkpoint inhibitors for immunotherapeutic management of glioma

Shang-Wen Lin, Cheng-Ping Yu, Jui-Chen Tsai, Yan-Jye Shyong *

*School of Pharmacy, College of Medicine, National Cheng Kung University, No. 1, University Road, Tainan City, 701, Taiwan*

ARTICLE INFO

*Keywords:*
Extracellular vesicles
Immune checkpoint inhibitors
Calcium phosphate particles
Glioma
Immunotherapy
Brain delivery

ABSTRACT

Glioma is a common primary malignant brain tumor with low survival rate. Immunotherapy with immune checkpoints inhibitors (ICI) can be a choice for glioma management, and extracellular vesicles (EVs) are recognized as a potential drug delivery system for various disease management due to their enhanced barrier permeation ability and immunomodulatory effect. The aim of this study is to develop ICI-loaded EVs (ICI/EV) that have sufficient efficacy in managing glioma. Calcium phosphate particles (CaP) were used to stimulate the secretion of EVs from murine macrophage cells. CaP conditioning of cells showed an enhanced amount of EVs secretion and macrophage polarization toward a proinflammatory phenotype. The CaP-induced EVs were shown to polarize macrophages into proinflammatory phenotype *in vitro*, as correlated with the conditioning method. ICI/EVs were successfully prepared with high loading efficiency using the sonication method. The EVs can be distributed throughout the entire brain upon intranasal administration and facilitate ICIs distribution into glioma lesion. Combinatory treatment with ICI/EVs showed benefit in glioma-bearing mice by reducing their tumor volume and prolonging their survival. Cytotoxic T cell infiltration, polarization of tumor-associated macrophage, and lower tumor proliferation were observed in ICI/EVs-treated mice. The developed ICI/EVs showed promise in immunotherapeutic management of glioma.

## 1. Introduction

Glioma is an aggressive primary malignant brain tumor characterized by the rapid growth of tumor cells and aggressive infiltration into other parts of the brain [1]. Glioblastoma is the most common glioma in adults, with a median survival time of less than 15 months and a 5-year survival rate lower than 3 % [2,3]. With the high recurrent rate of glioma, few drugs are available to achieve optimal therapeutic effects, and temozolomide is the only USFDA-approved drug for managing newly diagnosed glioblastoma. A new therapeutic strategy for managing glioma is of urgent need [2,4–6], and immunotherapy with immune checkpoint inhibitors (ICI) is a potential option.

USFDA-approved ICIs are monoclonal antibodies targeting CTLA-4, PD-1, or PD-L1 for managing melanoma and several solid tumors [4,7,8]. Preclinical studies of ICIs in glioma management have found benefits in prolonging survival in glioma-bearing mice [9,10], but current clinical trials have shown disappointing therapeutic outcomes of ICIs in glioma management [11–13]. With the unique barrier known as the blood-brain barrier (BBB) existing in the brain, the inefficient delivery of ICIs into the brain may be one reason for the treatment failure. A delivery system is necessary to overcome this obstacle for the efficient delivery of ICIs into the brain.

Extracellular vesicles (EVs) are cell-originated membrane vesicles that exist in various body fluids and culture media. They are composed of lipid bilayer, nucleic acids, and proteins derived from their parent cells. The EVs subtypes, including exosomes and microvesicles, are commonly investigated for therapeutic and drug delivery applications. They are recognized as safe drug delivery systems due to their cell-originated properties, which may reduce immunogenicity and long-term safety concerns. Their small size and lipophilic characteristic facilitate their trafficking through extracellular matrix and physical barriers, providing more efficient drug delivery to the target. EVs also possess characteristics similar to their parent cells; therefore, they can exert some disease management effect [14–17]. EVs derived from macrophages exhibit pro- or anti-inflammatory abilities, which are determined by the conditions of macrophages upon EVs secretion, and therefore they can facilitate tissue repair [18,19] or cancer management [20–22]. However, the low recovery of EVs is one of the limitations that

* Corresponding author.
*E-mail address:* bear901704@gs.ncku.edu.tw (Y.-J. Shyong).

https://doi.org/10.1016/j.mtbio.2024.101244
Received 7 February 2024; Received in revised form 13 August 2024; Accepted 13 September 2024
Available online 14 September 2024

hinder their application in both disease management and drug delivery. It is known that the generation of EVs correlates with the intracellular calcium content [23–25]. Therefore, enhancing the intracellular calcium level is a strategy to facilitate EVs secretion.

Calcium phosphate particles (CaP) are biomaterials commonly used as bone substitutes and drug or gene delivery systems [26]. They are biocompatible due to their similar composition to bone, and their biodegradability is based on different calcium-to-phosphate ratios [27]. Previous studies have indicated that CaP can stimulate EVs secretion from vascular smooth muscle cells [28,29], RAW264.7 and THP-1 cells [30], therefore CaP supplementation can be an optimal method to facilitate EVs secretion from cells.

Successful cases have been achieved with ICIs treatment in managing several cancers, but not in gliomas. Studies have found that EVs have potential in brain delivery of large molecular weight therapeutic agents in the management of brain inflammatory diseases and glioblastoma [31–33]. The application of EVs for ICIs delivery is therefore appropriate for accumulating ICIs in the brain to exert optimal therapeutic effect. The EVs also showed benefits in modulating the tumor microenvironment. For instance, EVs derived from M1 macrophages showed TAM repolarization ability that potentiates immunotherapeutic efficacy [20,34]. CaP is applicated as an EVs secretion stimulant in this study, and it has potential in influencing macrophage polarization. The purpose of this study is to prepare macrophage-derived EVs with CaP supplementation to obtain high amounts of EVs for the preparation of ICI-loaded EVs (ICI/EVs). The ICI/EVs are delivered into the brain for efficient glioma management. The effect of CaP on macrophage polarization was assessed along with the EVs' ability to induce TAM polarization. The ICI/EVs preparation method was established and optimized to achieve a high ICIs loading efficiency. An optimal delivery strategy was established for efficiently accumulating ICI/EVs in glioma lesions, and the therapeutic effect was evaluated in glioma-bearing animal models (Fig. 1).

## 2. Experimental methods

### 2.1. Materials

The polymer-precipitation reagent ExoQuick-TC and the acetylcholinesterase (AChE) assay EXOCET kit were purchased from System Biosciences (Palo Alto, CA, USA). Anti-mouse PD-L1 (catalog number BE0101, clone 10F.9G2) and anti-mouse CTLA-4 (catalog number BE0164, clone 9D9) were purchased from Bio X Cell (Lebanon, NH, USA). The FITC-preadsorbed rat monoclonal anti-mouse IgG1 (ab133859), mouse iNOS ELISA kit, and antibodies for immunoblotting, immunocytochemistry (ICC), and immunohistochemistry (IHC), were purchased from Abcam (Cambridge, UK). The rat and mouse IgG ELISA kits were obtained from Elabscience (Houston, TX, USA). Streptavidin peroxidase was obtained from Sigma-Aldrich (St. Louis, MO, USA). Mouse TNF-α, IL-1β, and IL-6 ELISA kits were purchased from BioLegend (San Diego, CA, USA). The recombinant mouse PD-L1/B7-H1 chimera protein (catalog number 1019-B7-100) and mouse IL-18 ELISA kit were purchased from R&D Systems (Minneapolis, MN, USA). Biotin-conjugated goat anti-rat IgG (H + L), mouse TGF-β ELISA kit, and antibodies for flow cytometry analysis were purchased from Thermo Fischer Scientific (Waltham, MA, USA). 3,3′,5,5′-tetramethylbenzidine (TMB) was purchased from Millipore (Burlington, MA, USA). D-luciferin, potassium salt was purchased from Gold Biotechnology (St. Louis, MO, USA). The RAW264.7 murine macrophage cell line was purchased from the Bioresource Collection and Research Center (BCRC, Hsinchu, Taiwan). The ALTS1c1 murine astrocytoma cell line was kindly provided by Professor Chi-Shiun Chiang in National Tsing-Hua University, Hsinchu, Taiwan. The GL261-luc murine glioblastoma cell line was purchased from Creative Biolabs (Shirley, NY, USA).

### 2.2. Preparation and characterization of CaP

The preparation of CaP followed the method previously published with slight modification [30]. $CaCl_2$ solution (11 mM, pH 9) was added to $Na_2HPO_4$ solution (66 mM, pH 11 adjusted with NaOH) at a rate of 1.0 ml/min. The pH value was adjusted during this process to reach pH 11 in the final mixture. The mixture was then centrifuged at 1500 × g for 30 min, and the precipitated CaP was washed once with 0.1 mM NaOH, followed by three washes with acetone, and finally washed with deionized water. The suspension was lyophilized to obtain CaP powder. This powder was mixed with 1 part of 1 mm stainless steel beads and 2 parts of deionized water in a volume ratio, and then milled using a tissue blender (Bullet Blender, Next Advance, USA) for 5 min. The recovery of CaP was estimated by comparing the weight before and after blending, and the resulting CaP suspension was autoclaved prior to use.

Particle characteristics, including size and zeta potential, were evaluated using dynamic light scattering (DLS, NanoPlus zeta/nano particle analyzer, Particulate Systems, USA). The morphology was examined under scanning electron microscope (SEM, HITACHI SEM SU8010, Hitachi, Germany). The solubility of CaP in pH 5 disodium citrate buffer was estimated by dissolving CaP in the buffer with

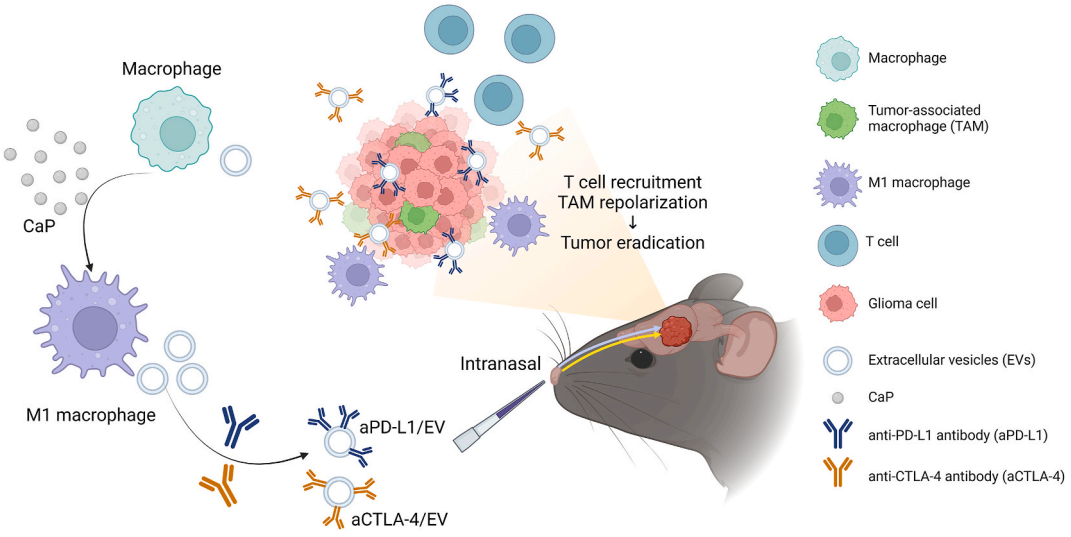


**Fig. 1.** Schematic illustration of EVs preparation in this study, which includes CaP supplementation and loading of ICIs onto the EVs for efficient intranasal delivery to glioma to exert an immunotherapeutic effect. The figure was created from Biorender.com.

vigorous shaking at room temperature until no particles were visible to the naked eye. FTIR (Nicolet 6700, Thermo Scientific, USA) and XRD (Ultima IV-9407F701, Rigaku, Japn) were applied for characterization.

### 2.3. Optimization of EVs preparation method

The RAW264.7 cells were seeded at a confluency density of $8.8 \times 10^6$ cells in 10 cm petri dish and allowed to grow for 24 h prior to conditioning. After conditioning, the conditioned medium was pipetted out and centrifuged (2000 × g, 4 °C, 30 min) to remove cell debris. This conditioned medium was then mixed with a polymer-precipitation reagent according to the manufacturer's instructions and incubated at 4 °C overnight. The mixture was subsequently centrifuged (10,000 × g, 4 °C, 60 min) to pellet the EVs, which were then resuspended in phosphate-buffered saline (PBS). The effects of CaP conditioning time, medium composition, and CaP concentration were evaluated to achieve a high EVs yield. EVs quantities were assessed using AChE assay.

### 2.4. Characterization of extracellular vesicles

Characterization of EVs followed the published MISEV guideline [35]. The particle size of EVs was characterized with nanoparticle tracking analysis (NTA, NanoSight LM10HS, Malvern Panalytical, UK). Morphology was observed with transmission electron microscope (TEM, JEM-2100F electron microscope, JEOL, Japan). Samples were negatively stained with 2 % uranyl acetated prior to TEM observation. Colocalization of IgG with EVs was determined using CLSM (Fluoview FV3000, Olympus, Japan). The FITC-conjugated rat IgG was sonicated with EVs and stained with PKH26 following the manufacturer's instructions to obtain IgG/EV. One drop of IgG/EV was added on to a glass slide and covered with a cover slip prior to examination.

Immunoblotting of EVs in comparison with RAW264.7 cell lysate was conducted to examine the protein constituent. EVs and RAW264.7 were lysed in RIPA lysis buffer and centrifuged to obtain the supernatant. Protein content was estimated with Bradford reagent, and 5 μg of total protein was loaded onto a polyacrylamide gel for electrophoresis separation. The protein was transferred onto 0.2 μm PVDF membrane and blocked with 5 % skim milk in PBST, followed by incubating with primary antibodies, including ALIX (ab186429, 1:1000), LAMP1 (ab208943, 1:1000), CD63 (ab217345, 1:1000), and β-actin (GTX109369, 1:1000) overnight at 4 °C. Goat anti-rabbit IgG H&L (ab205718,1:10,000) was used for blotting for 1 h at room temperature and developed with ECL for imaging (FluorChem R, ProteinSimple, CA, USA).

### 2.5. ICIs loading method and aPD-L1 binding affinity evaluation

Methods for optimizing the loading of ICIs are described in the Supporting Information. The established method for preparing ICI/EVs involved mixing 4 μg of aPD-L1 or aCTLA-4 with 0.7 ml of conditioned medium, respectively, and subjecting them to sonication on ice using a probe-type sonicator (MISONIX sonicator 3000, Misonix, USA). The condition was set at 3W output voltage for 3 cycles of 2 s pulse and 2 s pause. The samples were then left on ice for over 30 min prior to being mixed with polymer-precipitation reagent for ICI/EVs isolation following the manufacturer's instructions. The resulting pellets were resuspended in PBS, and the amounts of EVs were quantified using AChE assay and Bradford reagent. To determine the loading efficiency (LE) of ICIs in EVs, the ICI/EVs were lysed with RIPA lysis buffer, and the ICIs in the lysates were quantified using their respective ELISA that detect the IgGs of their host species. The LE of ICIs in EVs were calculated using the following formula:

$$\text{Loading efficiency (LE\%)} = \frac{\text{ICI amount in lysate}}{\text{Spiked ICI amount}} \times 100\%$$

The binding affinity of aPD-L1 was analyzed using a published ELISA method with slight modifications [36]. A volume of 100 μl of 2 μg/ml recombinant mouse PD-L1 chimera protein, dissolved in PBS, was coated onto a 96-well plate overnight at 4 °C. The wells were blocked for 1 h with PBST containing 0.1 % bovine serum albumin (BSA) at 37 °C with continuous shaking at 30 rpm, followed by incubation with either aPD-L1/EV samples or aPD-L1 standards in PBS for 2 h. Secondary biotin-conjugated goat anti-rat IgG (1:100,000) and streptavidin-peroxidase (1:50,000) were incubated for 1 h each. The wells were washed two to three times with PBST (PBS containing 0.05 % Tween20) prior to the next incubation step and were washed five times after the streptavidin-peroxidase incubation. The wells were brought to color with TMB, and the reaction was stopped with 2N sulfuric acid. The plates were then read using an ELISA reader (SpectraMax ID5, Molecular Devices, USA) to obtain the optical density at 450 nm.

### 2.6. Macrophage polarization test

For RAW264.7 cell polarization upon CaP or EV treatment, the cells were seeded at confluency density in 10 cm petri dishes or at a density of $1.2 \times 10^5$ cells in 6-well plates for 24 h. The cells were washed thrice with PBS prior to changing the medium. The medium contained 100 μg/ml of CaP or one hundred million EVs, while medium without CaP or EVs was used as the control. After 24 h of conditioning, the medium was pipetted out, centrifuged to remove cell debris, and refrigerated at −20 °C prior to analysis. The remaining cells were lysed with RIPA lysis buffer and analyzed with Bradford reagent. Cytokine concentrations in the medium and iNOS amount in cell lysates were evaluated using TNF-α, IL-1β, IL-6, IL-18, TGF-β, and iNOS ELISA kits following the manufacturer's instructions.

For ICC evaluation of iNOS expression, the cells were seeded in 35 mm μ-dishes (ibidi GmbH, Landkreis München, Germany), followed by the same experimental procedures described in the paragraph above. At designated time points, the medium was discarded, and the cells were washed once with PBS and fixed with 4 % paraformaldehyde for 30 min. After appropriate washing with PBS containing 0.3 % Triton X, the cells were blocked with 3 % BSA in PBS for 1 h iNOS primary antibody (ab3523, 1:100) was added and incubated overnight at 4 °C, followed by incubation with the secondary goat anti-rabbit antibody conjugated with Alexa 647 (ab150079, 1:1000) in the dark for 1 h in room temperature. The nuclei were stained with DAPI for 5 min and examined under fluorescent microscope (Automated fluorescence microscope BX61, Olympus Co., Japan). The cells were washed with PBST after each incubation steps.

### 2.7. ICI/EV permeation efficiency assessment

A trans-well system was established to evaluate the permeation enhancement effect of EVs. C2BBe1 cells were seeded at a density of $6 \times 10^4$ cells in cell culture inserts (Corning Inc., Corning, NY, USA) with a pore size of 0.4 μm and a permeation area of 0.9 $cm^2$. The culture inserts were placed in a 12-well culture plate, and the apical (A) and basolateral (B) sides were filled with 1 and 1.5 ml of culture medium, respectively. The medium on both sides was changed every other day, and trans-epithelial electric resistance (TEER) was measured for 20 days. The TEER was calculated with the following formula, in which $R_{Cell}$ indicated the electric resistance measured in the inserts with cells cultured and $R_{blank}$ indicated blank inserts without cells:

$$\text{TEER } (\Omega \times \text{cm}^2) = (R_{Cell}\text{-}R_{blank}) \times \text{permeation area}$$

The culture inserts were washed thrice with PBS prior to performing the permeation experiment. The B sides were filled with 2 ml of PBS, and the A sides were filled with 1 ml of 4 μg/ml free aPD-L1 or aPD-L1/EV in PBS. Samples were collected at 0, 1, 2, and 3 h by withdrawing 150 μl of solution from the B sides and replacing them with an equivalent volume of PBS. The aPD-L1 concentrations were evaluated with a rat IgG ELISA,

and the cumulative permeated amounts were calculated.

### 2.8. Establishment of orthotopic brain tumor model

Male C57/BL-6 mice were purchased from the National Laboratory Animal Center. Mice aged 6–9 weeks were applied for the experiments under protocols approved by the Institutional Animal Care and Use Committee (IACUC) of National Cheng Kung University (approval number: 111,084). They were housed in an environment with 40 % humidity, temperature of 22 ± 2 °C, a 12-h light-dark cycle, and free access to food and water. Mice were anesthetized with a mixture of Zoletile and Rompun prior to applying hair remover to the forehead. An incision was made with a scalpel blade, and a hole was drilled into the right side of the skull, 2 mm away from the midline and 1.5 mm posterior to the bregma. The needle was inserted into the brain to a depth of 2 mm, and $10^5$ GL261 or ALTS1c1 cells were pumped into the brain at a flow rate of 1 μl/min. The syringe was slowly removed, and the hole was sealed with bone wax prior to closing the wound with sutures.

### 2.9. In vivo ICI/EVs distribution in brain and tumor

The permeation enhancement effect of ICI/EVs was evaluated *in vivo* in both healthy and GL261-bearing mice. The mice were anesthetized with a mixture of Zoletile and Rompun prior to intranasal (IN) or retro-orbital (RO) administration of 10 μg FITC-conjugated IgG/EV to healthy mice and 60 μg of aPD-L1/EV to GL261-bearing mice, in comparison with free IgG or aPD-L1. Mice administered with PBS were used as controls. In RO injection, the drug was drawn into an insulin syringe and injected into the base of the eye while under anesthesia. In IN administration, 2 μl of liquid was administered into one nostril of the mice and left for 1 min prior to administering to the other nostril. This cycle was repeated until full dose was administered. To examine the distribution of IgG and aPD-L1, mice were sacrificed post drug administration. Whole brains were taken and cryo-sectioned into slices of 10 or 5 μm. For the examination of IgG distribution in healthy brains, slices were directly imaged to detect green fluorescence signals within the brain (FluorChem R, ProteinSimple, CA, USA). The fluorescence intensities of IgG were analyzed with Image J, and the cumulative intensity results were obtained by summing up the results of four consecutive slices from one mouse, representing the amount of IgG in one mouse brain. To examine the aPD-L1 distribution in GL261-bearing brains, the slices were stained with Alexa 488-conjugated goat-anti rat IgG (ab150165, 1:1000) to capture aPD-L1 and nuclei were stained with DAPI. The distribution of aPD-L1 within the brain was examined under CLSM (Fluoview FV3000, Olympus, Japan).

### 2.10. Therapeutic effect evaluation

Mice were initially implanted with orthotopic GL261 or ALTS1c1 tumors, and dosing began 3 days post tumor establishment, which was designated as day 0 of the experiment. The mice were randomly divided into five groups and treated with aPD-L1, aPD-L1/EV, aPD-L1 + aCTLA-4, or aPD-L1/EV + aCTLA-4/EV. Mice treated with PBS or receiving no treatment (designated as the control group) served as negative controls. The ICIs were IN administered on a daily basis for 3 doses, resulting in a total of 60 μg of respective ICIs in each treatment regimen. Tumor volumes were assessed with bioluminescence for GL261 tumors and tumor weight for ALTS1c1 tumors. Tumor bioluminescence was measured at designated time points by intraperitoneal injection of D-luciferin at dose of 150 mg/kg body weight. The bioluminescence was immediately examined with IVIS Spectrum In Vivo Imaging System (Perkin Elmer, MA, USA). Baseline bioluminescence was determined on day 0 prior to dosing. The total bioluminescence flux from each mouse's tumors at designated times was evaluated, and tumor growth was expressed as fold changes from the total flux measured at day 0. Survival duration was assessed by daily recording of body weight for 35 days. Mice were humanely euthanized when body weight loss exceeded 20 % or when apparent weakness or disability was observed.

### 2.11. Immunohistochemistry staining

Mice were euthanized on day 30 by cervical dislocation. The tumors were isolated and cryo-sectioned into 5 μm slices. The slices were fixed with cold acetone, followed by permeabilization with 0.2 % Triton-X in PBS for 15 min. The slices were then blocked with 3 % BSA for 30 min, and subsequently incubated overnight at 4 °C with anti-mouse F4/80 (ab111101, 1:100) or CD8 (ab217344, 1:500) primary antibodies, followed by incubation with Alexa 488-conjugated secondary antibodies (ab150077, 1:1000) for 1 h. For F4/80-stained slices, an additional step involved blocking and incubating with anti-mouse iNOS (ab3523, 1:50), followed by Alexa 647-conjugated secondary antibodies (ab150079, 1:200) under the same incubation conditions. The nuclei were counterstained with DAPI and examined under a fluorescence microscope. To examine tumor proliferation, the slices were permeabilized and blocked, followed by incubation with anti-mouse Ki67 (ab15580, 5 μg/ml) primary antibodies. The slices were then treated with 0.3 % $H_2O_2$ to block endogenous peroxidase activity for 15 min, followed by incubation with HRP-conjugated secondary antibodies (ab6721, 1:1000). The slices were brought to color with DAB substrate (ab64238), and nuclei were counterstained with hematoxylin (Leica biosystems, IL, USA), followed by observation with a microscope.

### 2.12. Flow cytometry analysis of tumor-associated immune cells

Mice that received full treatment were sacrificed at day 19 and 26 in ALTS1c1-and GL261-bearing mice, respectively, to obtain tumor. The tumors were immersed and minced in RPMI 1640. After removing the supernatant by centrifugation at 5000 rpm for 3 min, the tissue was treated with a digesting buffer containing 1 kU/ml of collagenase type 4 and 2 U/ml deoxyribonuclease I from bovine pancreas in RPMI 1640, and then incubated at 37 °C for 10 min. The digested tissue was passed through a 70 μm cell strainer and washed with PBS, followed by centrifugation at 5000 rpm for 3 min to obtain a cell pellet. RBC lysis buffer was added and incubated at room temperature for 1 min, followed by centrifugation to pellet the cells. The cells were washed once with PBS and the cell count was adjusted to prepare $10^8$ cells in 100 μl PBS. The cells were first stained with fixable viability dye for 30 min at 4 °C, and then washed once with 1 ml flow cytometry staining buffer (FACS buffer). The cells were then blocked with CD16/CD32 monoclonal antibody for 10 min at 4 °C, followed by incubating with surface antibodies for 30 min at 4 °C. The cells were fixed and permeabilized for 30 min and 15 min, respectively, at room temperature. The cells were then stained with intracellular antibodies in permeabilization buffer for 30 min at 4 °C. After appropriate washing with permeabilization buffer, the cells were resuspended in 100 μl FACS buffer and stored at 4 °C prior to analysis (Attune NXT Flow Cytometer, Invitrogen, USA).

### 2.13. Statistical analysis

Results were expressed as mean ± standard deviation (SD) in *in vitro* studies and mean ± standard error of the mean (SEM) for *in vivo* studies. One-way ANOVA with Bonferroni post hoc test was applied for comparison of means between groups. General linear model (GLM) was applied for comparisons of EVs secretion stimulation trend with CaP supplementation, and tumor volume change between groups. Survival between groups were analyzed with Kaplan-Meier method with log rank test. Differences were considered significant at $p < 0.05$ and all computations were performed with SPSS 22.0.

## 3. Results and discussion

### 3.1. CaP induced EVs secretion and macrophage polarization

The CaP prepared in this study exhibited particle characteristics with a size of around 1.5 μm and a negative surface charge. A PDI around 0.4 indicated a broad particle size distribution for the CaP suspension (Fig. 2(A)). The CaP displayed particulate characteristics with an irregular morphology under SEM (Fig. 2(B)). The solubility of CaP in pH 5 buffer was estimated to be 3.8 ± 0.2 mg/g. The FTIR and XRD spectra were similar to those in previous research [37,38], indicating the successful preparation of CaP (Fig. S1).

The feasibility of using CaP as EVs secretion stimulant was assessed. A higher amount of EVs secretion was observed in CaP-treated RAW264.7 cells throughout the 48-h experiment compared to cells without CaP treatment, the latter being designated as the blank group (Fig. 2(C)). EVs were secreted from the cells and reached a steady state 12 h post CaP treatment, peaking at 48 h. The effects of the medium and the amount of CaP supplementation on EVs secretion were assessed. PBS supplemented with CaP showed a higher EVs secretion compared to DMEM (Fig. S2), and Fig. 2(D) indicated that conditioning cells with 100 μg/ml CaP in PBS resulted in a higher amount of EVs secretion. Increasing the amount of CaP did not further facilitate EVs secretion, potentially due to cell necrosis from excessive CaP treatment [39].

Cytokine concentrations in the conditioned medium and iNOS expression, as compared between conditioning methods, are analyzed and shown in Fig. 2(E). The DMEM, which is the normal culture condition for RAW264.7, was utilized as the control for the other groups. Cells treated with CaP were compared with those without CaP treatment as well. While TNF-α concentrations were comparable between groups, PBS- and PBS + CaP-conditioning led to significantly higher IL-1β, IL-6, IL-18, and lower TGF-β secretion compared to DMEM-conditioning. CaP-supplemented PBS showed a significantly higher IL-1β and IL-18 secretion compared to PBS group. Additionally, PBS + CaP group displayed higher iNOS expression than PBS and DMEM groups, although the difference was not significant. ICC images of iNOS expression in macrophages 4 h post-conditioning were compared, revealing that macrophages conditioned with CaP showed more iNOS expression than those conditioned with DMEM and PBS (Fig. 2(F)). Based on these findings, it can be deduced that macrophages can polarize into proinflammatory phenotype when conditioned with CaP-containing PBS. To further evaluate the ability of CaP in inducing macrophages polarization, a CaP-containing DMEM group was compared with DMEM and showed in Fig. S3. While not as significant compared to PBS-conditioning, the CaP-containing DMEM group showed significantly more IL-18 and less TGF-β secretion, along with more iNOS expression, compared to DMEM group, indicating the proinflammatory ability of CaP in different medium. The expression tendency was not consistent between cytokines in different groups, it can be due to the different mechanisms that triggered the differences in expression and secretion of cytokines [40].

Simultaneous enhancement of EVs secretion amount and polarization of macrophages into proinflammatory phenotype was achieved by conditioning cells with CaP. This could be attributed to the elevation of intracellular calcium levels, which triggered various cellular responses, including the secretion of cellular materials like cytokines [41] and EVs [23]. Macrophage phagocytosis is particle size-dependent, with diameters of 2~3 μm are more readily taken up [42,43]. The size of CaP in this research was optimal for macrophage phagocytosis, and the engulfed CaP can be transferred into phagosomes and fused with lysosomes to become phagolysosomes. The low pH environment within phagolysosomes can contribute to CaP degradation, leading to increased

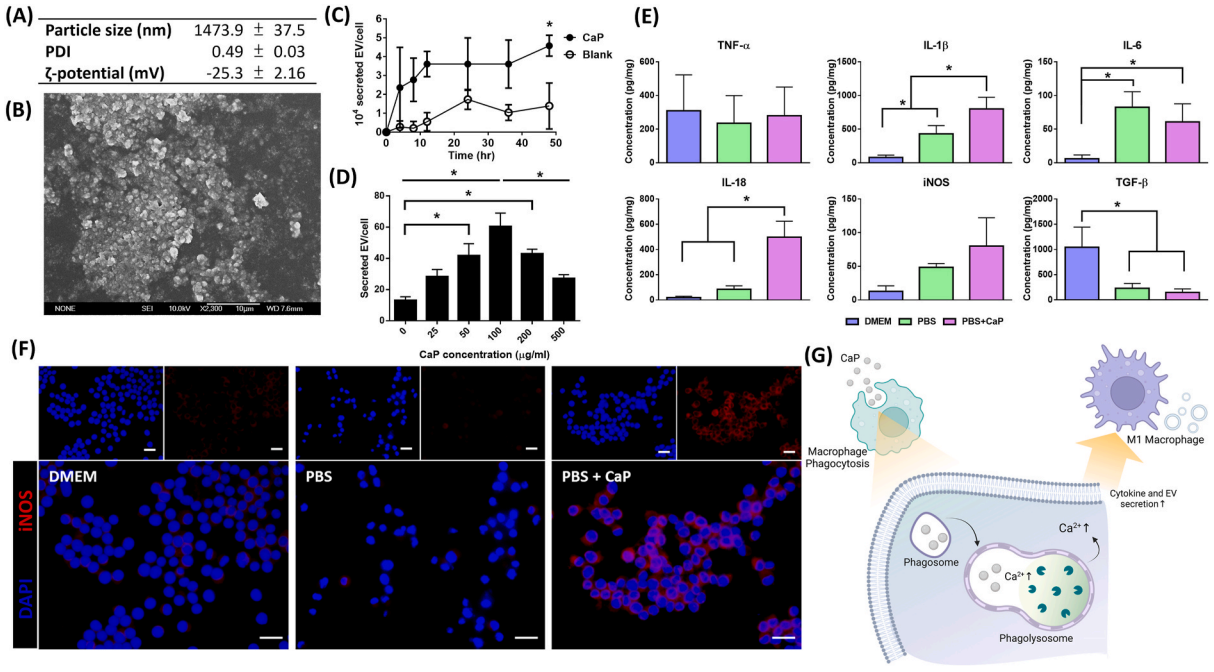


**Fig. 2.** Characteristics of CaP and its influence on EVs secretion and macrophage polarization. (**A**) DLS analysis results of particle size and ζ-potential of CaP. (**B**) SEM image of CaP. (**C**) Comparison of EVs secretion from RAW264.7 cells with and without 500 μg/ml CaP supplementation. (**D**) EVs secretion comparison from cells conditioned with varying CaP concentrations. (**E**) Cytokines concentrations in the conditioned medium and iNOS expression in RAW264.7 cells were analyzed with their respective ELISA and concentrations were adjusted based on the total protein amounts of cells, which were quantified with Bradford reagent. (**F**) ICC results of iNOS expression in RAW264.7 cells post 4 h conditioning. The red color indicates iNOS expression, and blue denotes nuclei stained with DAPI. Scale bar: 20 μm. (**G**) A scheme illustrating influence of CaP on macrophages (created from Biorender.com). Statistics for (**C**) were obtained from GLM with Bonferroni post hoc test, and the asterisk indicate a significant difference compared to the Blank group. Statistics for (**D, E**) were obtained from one-way ANOVA with Bonferroni post hoc test. Asterisks represent significant differences compared to the indicated groups. All data are expressed as mean ± SD with n = 3, and significance was defined as $p < 0.05$.

osmotic pressure from the release of calcium and phosphate ions. This results in the destruction of the phagolysosome [39,42] and an enhanced intracellular calcium level (Fig. 2(G)). This phenomenon is unlikely exerted by enhanced extracellular calcium concentration since the calcium levels are tightly regulated within cells, which makes adjusting intracellular calcium levels inefficient [32,44]. Other than CaP administration, cellular stress like nutrient deprivation with PBS conditioning, can also result in enhanced intracellular calcium level that facilitate cytokines secretion [45,46], and glucose starvation was suggested to result in cellular secretion of IL-6 and IL-8 [47]. While cells respond differently toward stress, the starvation of cells under PBS culture can be an explanation of the differences in cytokines secretion compared to DMEM.

In this study, a change in macrophage characteristics towards CaP conditioning was observed. CaP supplementation not only enhanced the secretion of EVs but also induced the macrophages polarization, and PBS conditioning potentiated this effect. Agents like lipopolysaccharide (LPS) and IFN-γ are commonly used to polarize macrophages into the proinflammatory phenotype. LPS is a pyrogen undesirable in pharmaceutical preparations, and IFN-γ can induce a strong autoimmune response. Both agents can remain in the EVs products when used for M1 macrophage polarization. The established CaP conditioning method in this study offers a potential alternative for simultaneously polarizing macrophages and enhancing EVs secretion without the residue of the aforementioned agents. While CaP administration resulted in increased secretion of some proinflammatory cytokines from RAW264.7 cells, it is still a different mechanism from infection or autoimmune pathogenesis pathways that result in increased expression of iNOS and secretion of TNF-α, IL-1β, IL-6, and IL-18 along with decreased secretion of anti-inflammatory TGF-β [48]. This can be supported by a previous study showing the efficient induction of TNF-α and IL-6 mRNA expression with LPS treatment on RAW264.7 cells [34]. The insignificant alteration of TNF-α, the main cytokine released immediately in response to pathogen infection [48], indicated the different reaction of RAW264.7 when encountered with CaP rather than LPS. Despite the unique pattern of proinflammatory cytokines secretion, the PBS + CaP treatment of RAW264.7 cells showed proinflammatory phenotype polarization tendency, which was supported by the higher iNOS expression and lower anti-inflammatory TGF-β secretion observed in this study, and the CaP supplementation potentiated this effect as compared to the PBS group (Fig. 2(E)–Fig. S3). Summing up the results of EVs secretion rate as well as cytokines and iNOS expression, the EVs preparation method in this study was established by conditioning RAW264.7 cells with PBS containing 100 μg/ml CaP for 24 h to achieve high EVs secretion amount and to ensure the origin of EVs from cells of proinflammatory phenotype. These will be beneficial in achieving sufficient drug loading and retain the proinflammatory characteristics of EVs for therapeutic application.

### 3.2. EVs exhibited exosome-like characteristics and capable for loading of ICIs

The EVs prepared in this study, derived from CaP-conditioned macrophages (EV w/CaP), were characterized by their size, morphology, and protein composition as suggested in the MISEV2018 guideline [35]. The average size of EV w/CaP analyzed with NTA was 161.7 ± 22 nm, and its spherical vesicular morphology similar to EVs prepared with polymer precipitation method [49], was identified under TEM (Fig. 3(A)). The slightly decreased particle size observed under TEM may be due to the differences in sample preparation for observation, and similar phenomenon was observed in lipid nanoparticles analyzed with DLS and TEM as well [50]. Immunoblotting of EV w/CaP showed the expression of LAMP1, ALIX and CD63, indicating their endolysosomal and phagolysosomal biogenesis pathways (Fig. 3(B),

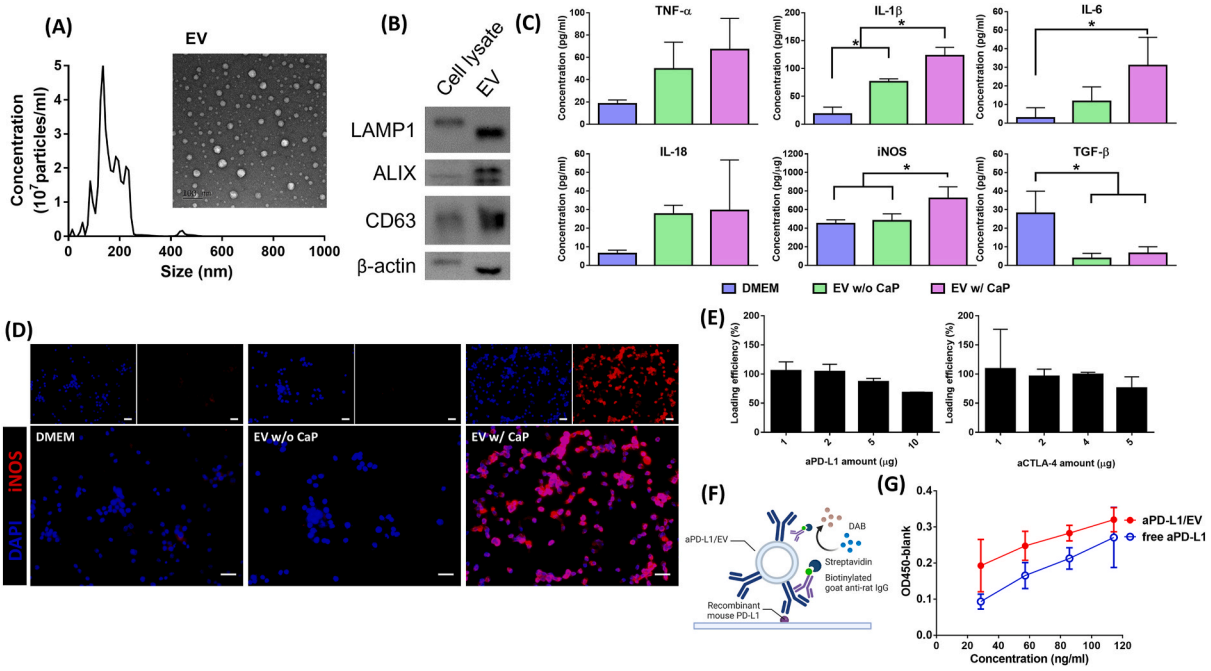


**Fig. 3.** EVs characteristics and ICI/EVs preparation method establishment. (**A**) Particle size of EVs was analyzed with NTA, and morphology was observed with TEM. (**B**) Protein markers in both RAW264.7 cell lysate and EVs were examined through immunoblotting. (**C**) Cytokines concentrations in the culture medium and iNOS expression post EVs treatment were analyzed with respective ELISA. (**D**) Immunocytochemistry evaluation of iNOS expression in RAW264.7 cells post EVs treatment in comparison to DMEM-cultured cells. Scale bar: 50 μm. (**E**) ICIs spiking amount in 0.7 ml of conditioned medium was evaluated by the LE of aPD-L1 and aCTLA-4. (**F**) Scheme of ELISA for aPD-L1/EV binding affinity evaluation (created from Biorender.com). (**G**) The binding affinity of aPD-L1/EV toward PD-L1 was analyzed with ELISA in comparison with free aPD-L1 to ensure the preservation of ICI function post preparation. Statistics in (**C**) were obtained from one way ANOVA with Bonferroni post hoc test. Asterisks represented significant differences between indicated groups, and significance was defined as $p < 0.05$. All data were expressed as mean ± SD with n = 3 in (**C, E**) and n = 5 in (**G**). LE: loading efficiency.

Fig. S4). The particle size and the expressed proteins indicated the possible exosome entity of the prepared EVs, demonstrating that the conditioning method established in this study stimulated the secretion of exosomes from cells via the known endolysosomal pathway and the proposed CaP-associated phagolysosomal pathway.

EVs are known for their intercellular communication and microenvironment modulation ability [51]. Based on the findings that CaP induced macrophage polarization and EVs secretion (Fig. 2), the potential macrophage polarizing ability was compared between EV w/CaP and EVs derived from cells without CaP treatment (EV w/o CaP). Fig. 3 (C) showed that RAW264.7 cells treated with EV w/CaP tended to polarize to proinflammatory phenotype compared to DMEM and EV w/o CaP groups, as significantly greater amounts of proinflammatory IL-1β and IL-6, as well as higher secretion amount of TNF-α were observed. Consistent with the increased proinflammatory cytokine secretion, significantly less anti-inflammatory TGF-β secretion and more iNOS expression were also observed in cells treated with EV w/CaP, and ICC images also displayed more intracellular iNOS expression in EV w/CaP-treated cells (Fig. 3(D)), confirming the proinflammatory polarization of RAW264.7 cells treated with EV w/CaP. Compared to the DMEM group, the EVs-treated cells showed a different extent of proinflammatory phenotype polarizing tendency, with EV w/CaP treatment exhibited the most significant effect. The proinflammatory characteristics of EV w/CaP may originated from their cargos derived from parent cells, including the cytokines, that contributed to the polarization of macrophage into the proinflammatory phenotype similar to the cells secreting EVs [19,28,34]. While TNF-α, IL-1β, iNOS, and TGF-β showed similar secretion or expression trends compared to the parent RAW264.7 cells treated with CaP, differences in IL-6 and IL-18 secretion trends were observed in EV w/o and w/CaP that are not comparable with the CaP treatment results (Figs. 2(E) and 3(C)). The differences in IL-6 levels between EV w/o CaP and EV w/CaP, as well as between PBS and PBS + CaP groups, may be overlooked due to their insignificant differences. Another possible reason can be the complex intracellular cargo transportation and sorting while secreting EVs that led to the different reactions of cells toward EVs and CaP treatment. While the ability of EVs in remodeling diseased environment were documented, more research should be conducted to elucidate the underlying mechanism that precipitate to the observed results.

The ICI/EVs preparation method was established by first comparing the LE of aPD-L1 in EV w/CaP with three different loading methods. Table S1 showed that the incubation method led to a relatively lower LE of aPD-L1 in EVs, whereas sonication resulted in a higher LE compared to the freeze/thaw method. To further confirm the suitability of sonication in ICIs loading, FITC-conjugated rat IgG was loaded into PKH26-stained EVs with sonication method, and the respective fluorescence was well-localized (Fig. S5). The sonication method was chosen for the loading of ICIs due to its high aPD-L1 LE, and the sonication condition was further optimized based on the number of sonication cycles and the amount of ICIs spiked. Under the same output voltage, increased sonication cycles had a small influence on EVs concentrations and aPD-L1 LE, but they might lead to a lower total protein concentration, indicating the loss of proteins and their functions during preparation (Fig. S6). The maximum LE of ICIs into EV could be achieved by spiking approximately 4 μg of aPD-L1 or aCTLA-4 into 0.7 ml conditioned medium, as the LE of ICIs was saturated at 4–5 μg (Fig. 3(E)). Based on these results, the ICIs loading method was established by sonicating 4 μg ICIs with 0.7 ml of conditioned medium for 3 cycles. Under this condition, the loading amount of ICIs in EVs was 1.03 ± 0.15 and 1.37 ± 0.04 μg/$10^7$ EVs for aPD-L1 and aCTLA-4, respectively. The particle size and TEM image of aPD-L1/EV were analyzed and shown in Fig. S7.

To confirm the preservation of ICIs' function post loading, the binding affinity of aPD-L1/EV toward PD-L1 was evaluated with ELISA in comparison with free aPD-L1 (Fig. 3(F)). The result in Fig. 3(G) showed a slightly enhanced binding affinity of aPD-L1/EV toward PD-L1 compared to free aPD-L1 but without a significant difference, indicating the preserved target binding ability of ICIs post preparation. The enhanced binding affinity detected in aPD-L1/EV may be due to the high LE of aPD-L1 on EVs that attracted more secondary antibodies. Similar results were also obtained with the ICC results of *in vitro* aPD-L1/EV distribution toward GL261 cells, where aPD-L1 was more readily distributed to GL261 cells with the aid of EVs compared to free aPD-L1 (Fig. S8). Based on these results, the ICI/EVs preparation method was established with high ICIs loading efficiency and preserved ICIs target binding ability.

### 3.3. EVs facilitated ICIs delivery with enhanced barrier permeation rate and distribution into orthotopic glioma

Enhanced barrier permeability and efficient delivery represent desirable characteristics of EVs for drug delivery applications [51]. *In vitro* and *in vivo* assessments were conducted to evaluate the feasibility of using EVs for delivering ICIs to brain tumors. C2BBe1, a CaCo-2 clone commonly employed for intranasal and barrier permeation studies [52], was utilized in this study to assess the barrier permeability of ICI/EVs (Fig. 4(A)). TEER was recorded to ensure barrier integrity and to monitor monolayer formation, with a TEER value of 455.4 ± 4.8 Ω × $cm^2$ recorded on day 20 (Fig. S9). The permeation results in Fig. 4(B) demonstrated that aPD-L1/EV could readily permeate through the C2BBe1 barrier, exhibiting around a 60 % enhancement in permeated aPD-L1 compared to the free aPD-L1-administered group. This outcome indicated the permeation-enhancing effect of EVs, which could be advantageous for ICIs delivery across intact barriers.

*In vivo* studies were performed to assess the delivery efficiency of ICIs with EVs and to determine the optimal delivery method achieving the highest brain accumulation of ICIs. The RO and IN methods were compared with FITC-conjugated IgG as a model drug. In order to increase the accessibility of the ICIs to enter the brain systemically, the RO route was chosen over the tail vein injection due to its close proximity to the brain and the avoidance of first-pass metabolism [53]. IN administration is recognized for its efficient delivery and accumulation of protein drugs into the brain compared to systemic administration due to the higher permeability of nasal epithelium compared to the dense BBB [54]. Fig. 4(C) illustrated that IN administration of IgG/EV resulted in a significantly higher cumulative fluorescence intensity of IgG, with a 67–130 % enhancement compared to the other groups. RO administration of IgG/EV and free IgG exhibited limited brain accumulation effects, potentially due to the rapid systemic distribution of the administered substances rather than proximal entry into the brain. However, no difference was observed between RO and IN administration of free IgG, and higher IgG signals were observed in IgG/EV-administered groups compared to free IgG groups, irrespective of the delivery route, indicating the barrier permeation enhancement effect of EVs. The IN administration method was selected as the preferred drug delivery route for further *in vivo* studies due to its effective distribution and delivery of IgG/EV within the brain.

The distribution of aPD-L1 within orthotopic glioma brain tissue after IN administration was also evaluated. Fig. 4(D) showed more significant aPD-L1 distribution within the tumor compared to the administration of free aPD-L1, which was primarily located at the tumor margin. This result indicated that EVs facilitated the distribution of ICIs within the brain and tumor, while preserving the targeting ability of aPD-L1 upon loading into EVs. Efficiently delivering ICIs to the brain could also reduce safety concerns. Plasma concentration of IL-6, an indicator of ICIs-related adverse events (irAEs) [55,56], was significantly higher after intravenous (IV) injection of aPD-L1 + aCTLA-4 compared to that administered intranasally (Fig. S10). Notably, two out of the six mice in the IV aPD-L1 + aCTLA-4 group died shortly after dosing, indicating the potential risk of irAEs upon IV administration of ICIs. In contrast, IN administration of ICIs showed a slightly but insignificantly increase in IL-6 plasma concentration compared to the control group. It can be concluded that IN administration led to a constrained distribution

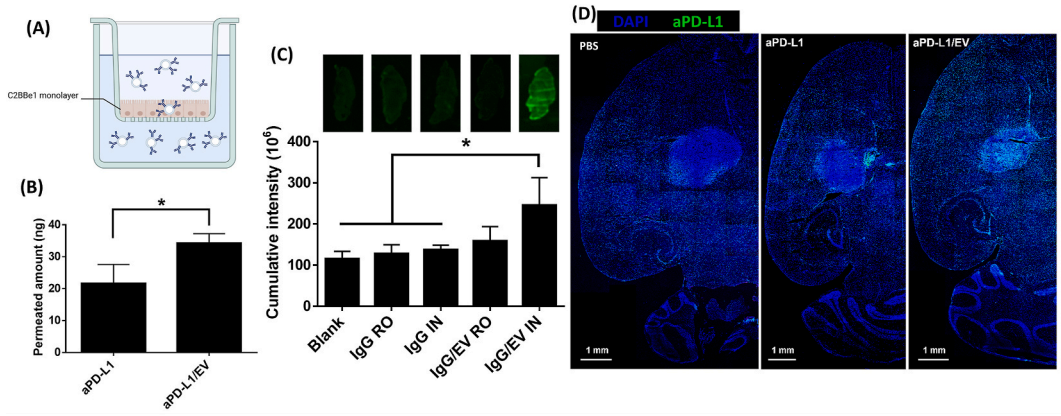


**Fig. 4.** Barrier permeation enhancement effect of EVs and efficient delivery of aPD-L1/EV into brain. (**A**) Scheme of the *in vitro* barrier permeation test with C2BBe1 trans-well system (created from Biorender.com). (**B**) Amounts of permeated aPD-L1 with free aPD-L1 or aPD-L1/EV administration through the C2BBe1 barrier. (**C**) Comparison of drug delivery efficiency with RO or IN administration of FITC-conjugated IgG or IgG/EV. The upper column displays the fluorescence of IgG within brain sections, and the lower column shows the cumulative fluorescence intensity of brain sections. (**D**) Distribution of aPD-L1 in GL261 tumor-bearing mice. Green fluorescence indicates aPD-L1, and nuclei were stained with DAPI. Statistics in (**B, C**) were conducted by one-way ANOVA with Bonferroni post hoc test. Asterisks represent a significant difference between indicated groups, with significance defined as $p < 0.05$. Data were presented as mean ± SD with n = 3.

and reduced systemic exposure of ICIs, thereby establishing a safe and efficient delivery strategy for ICI/EVs administration. In summary, EVs serve as a suitable delivery system for ICIs, preserving their targeting ability and efficiently permeating through biological barriers to deliver ICIs to the brain and tumor with reduced safety concern.

### 3.4. *ICI/EVs facilitated tumor volume reduction and prolonged survival in glioma-bearing mice*

The therapeutic effects of ICI/EVs on tumor-bearing mice were evaluated using two orthotopic glioma models (Figs. 5 and 6). The experimental scheme was illustrated in Fig. 5(A). GL261 tumor volumes were analyzed, and Fig. 5(B and C) shows a continuous enlargement of tumor volumes, characterized by rapid growth from day 0 to day 11, followed by a slight decrease on day 25 in the PBS, aPD-L1, aPD-L1/EV, and aPD-L1 + aCTLA-4 groups. Mice treated with aPD-L1/EV + aCTLA-4/EV showed minimal tumor volume changes during the 25-day observation. This trend was significantly different from the PBS and aPD-L1-treated mice and displayed a 5.5- to 9.5-fold reduction in tumor volume on day 25 compared to the other treatment groups. A slower

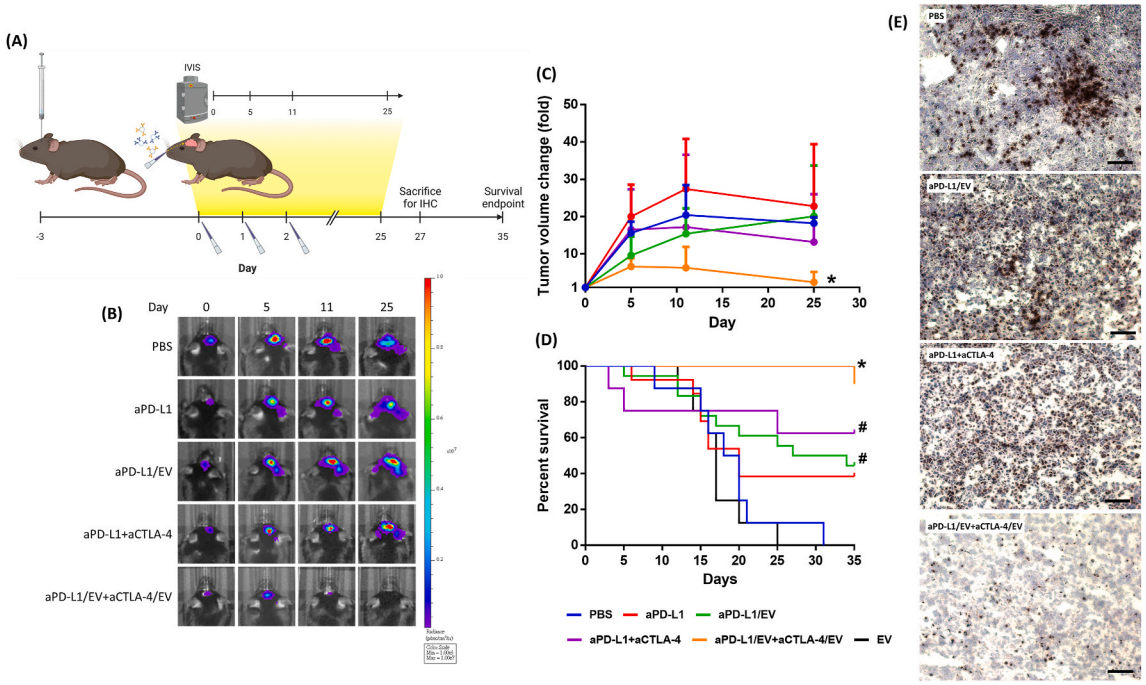


**Fig. 5.** Therapeutic effect of ICI/EVs in managing orthotopic GL261 tumors. (**A**) Schematic of experimental procedures for GL261 tumor management (created from Biorender.com). (**B, C**) Tumor volumes were evaluated with IVIS, and representative images are shown in (**B**). Changes in tumor volume were calculated based on the total flux observed on day 0 (**C**). (**D**) The survival of orthotopic GL261 tumor-bearing mice post-treatment was analyzed. The aPD-L1/EV + aCTLA-4/EV group demonstrated an extended survival time compared to other treatment groups. (**E**) Ki67 staining of GL261 tumors. Scale bar: 50 μm. Statistics for (**C**) were obtained from GLM with Bonferroni post hoc test, and for (**D**) from the Kaplan-Meier survival analysis with log rank test. The asterisk in (**C**) indicates a significant difference from the PBS and aPD-L1 treatments. In (**D**), the asterisk and hash signs represent significant difference from all treatment groups and from the PBS group, respectively. Significance was defined as $p < 0.05$. Data are presented as mean ± SEM with n = 4 in (**C**) and in (**D**) with n = 8~18.

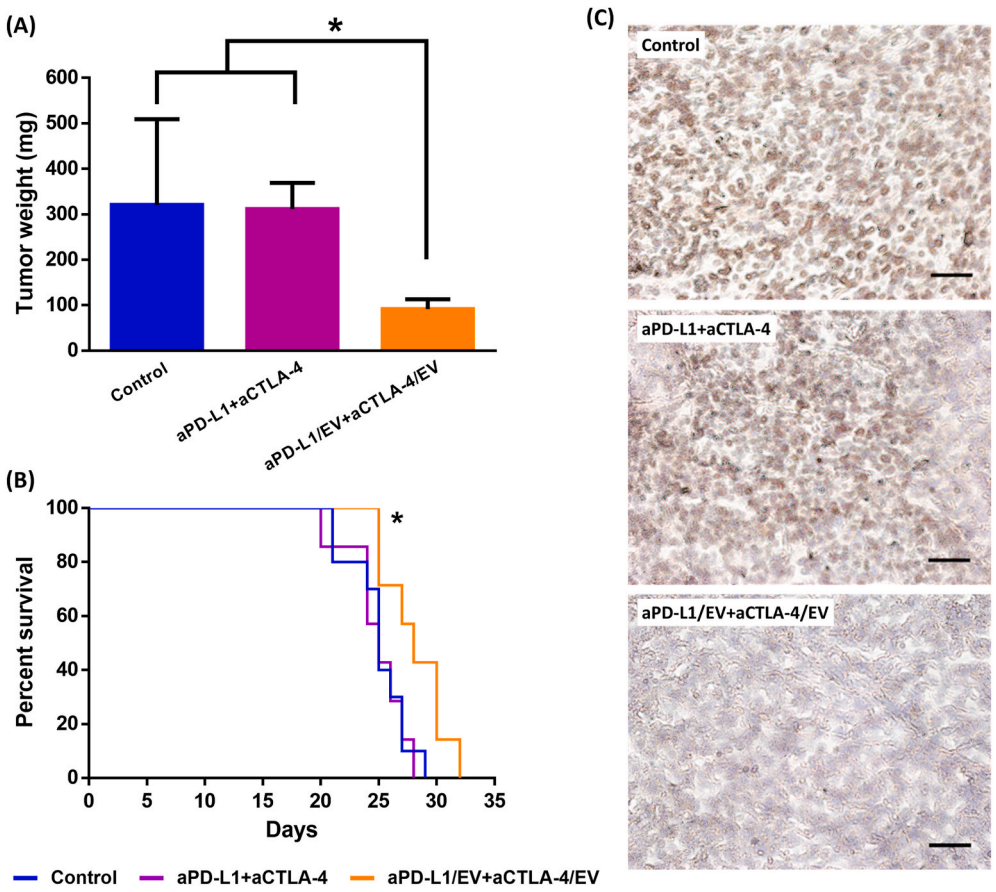


**Fig. 6.** Therapeutic effect of ICI/EVs in managing orthotopic ALTS1c1 tumors. (**A**) Tumor weights were examined on day 19, revealing reduced tumor weights with aPD-L1/EV + aCTLA-4/EV treatment. (**B**) Survival of orthotopic ALTS1c1 tumor-bearing mice post treatments, showing prolonged survival duration with aPD-L1/EV + aCTLA-4/EV treatment. (**C**) Ki67 staining of ALTS1c1 tumors showed no proliferating cells with aPD-L1/EV + aCTLA-4/EV treatment. Scale bar: 50 μm. Statistics for (**A**) were obtained from one-way ANOVA with Bonferroni post hoc test, and for (**B**) from the Kaplan-Meier survival analysis with the log rank test. The asterisks in (**A, B**) indicate a significant difference from the other groups, with significance defined as $p < 0.05$. Data are presented as mean ± SEM with n = 5 in (**A**), n = 7 in aPD-L1 + aCTLA-4, aPD-L1/EV + aCTLA-4/EV, and n = 10 in control group in (**B**).

initial tumor volume enlargement rate was observed in the ICI/EV groups (aPD-L1/EV and aPD-L1/EV + aCTLA-4/EV) than in their respective free ICI groups (aPD-L1 and aPD-L1 + aCTLA-4). Hematoxylin and eosin staining of tumor-bearing brains was also assessed. The tumor volume correlated well with the findings from IVIS, confirming that the tumor reduction effect was due to the therapeutic impact of ICI/EVs and not from luciferase loss (Fig. S11). The survival of GL261-bearing mice post-treatment showed that both PBS and EVs-treated mice had shorter survival durations, with median survival times of 19 and 17 days, respectively. All mice in these groups died within the 35-days study period. Comparable survival rates were observed between the aPD-L1 and aPD-L1/EV treatments in the first 15 days. However, the aPD-L1/EV treatment led to a longer median survival time (30.5 days) than the aPD-L1 treatment (20 days). This highlights the benefits of aPD-L1/EV in extending survival compared to free aPD-L1. Combination treatments with ICIs showed longer survival durations than the single aPD-L1 treatment, with undefined median survival times in both groups. Early death was observed with the aPD-L1 + aCTLA-4 treatment, where the mice experienced rapid body weight loss and met the humane sacrifice criteria. On the contrary, only one mouse in the aPD-L1/EV + aCTLA-4/EV group died on day 35. The statistical results revealed that the aPD-L1/EV + aCTLA-4/EV treatment significantly extended survival compared to all other treatment groups, and the survival durations of aPD-L1/EV and aPD-L1 + aCTLA-4 were significantly longer than that of PBS (Fig. 5(D)). The Ki67 staining results showed minimal positive staining for proliferating cells in glioma tissue treated with aPD-L1/EV + aCTLA-4/EV, in contrast to other treatment groups and the PBS control (Fig. 5(E)). The lowest proliferation index was also found in mice underwent aPD-L1/EV + aCTLA-4/EV treatment (Fig. S12(A). This finding correlates with the tumor volume and survival analysis, suggesting that the combination of ICI/EVs treatment inhibits tumor proliferation, leading to optimal therapeutic outcomes in the GL261 model.

Based on the therapeutic results observed in GL261-bearing mice, ALTS1c1 was applied to evaluate the therapeutic effect and further confirm the efficacy of ICI/EVs. Only combinatory ICIs treatments were examined, based on the finding that this treatment resulted in better therapeutic outcomes as observed in GL261 (Fig. 6). In ALTS1c1-bearing mice, the aPD-L1/EV + aCTLA-4/EV group exhibited significantly smaller tumor weights, with a 2.5-fold reduction at day 19, compared to the aPD-L1 + aCTLA-4 and control groups, both of which had comparable tumor weights (Fig. 6(A)). A significantly prolonged survival duration was observed in the aPD-L1/EV + aCTLA4/EV group. The median survival time for the control, aPD-L1 + aCTLA-4, and aPD-L1/EV + aCTLA-4/EV groups were 25, 25, and 28 days, respectively (Fig. 6 (B)). Fewer Ki67-positive cells were observed in tumors treated with aPD-L1/EV + aCTLA-4/EV, along with the lowest proliferation index compared to the control and aPD-L1 + aCTLA-4 groups (Fig. 6(C)–Fig. S12(B)). In summary, the aPD-L1/EV + aCTLA-4/EV treatment led to tumor reduction, extended survival, and inhibited tumor cell proliferation in both glioma mouse models. The efficient delivery of ICIs into the brain, facilitated by EVs, can be the reason for the observed optimal therapeutic effects.

### 3.5. Efficient delivery of ICI/EVs facilitated immune modulation in tumor microenvironment

Immune cells, including cytotoxic T cells and M1 macrophages, were analyzed with IHC and flow cytometry in both GL261 and ALTS1c1 tumors to further confirm the immunotherapeutic effects exerted by ICI/EVs (Figs. 7 and 8). $CD8^+$ cytotoxic T cells were observed in IHC results with ICIs and ICI/EVs treatment compared to PBS or control groups in both glioma models. aPD-L1/EV + aCTLA-4/EV treatment resulted in greater infiltration of cytotoxic T cells compared to the other treatment groups (Figs. 7(A) and 8(A)). The tumor-associated macrophages (TAM) in both glioma models showed a tendency towards M1 phenotype polarization with EVs-administered groups, specifically the aPD-L1/EV and aPD-L1/EV + aCTLA-4/EV treated mice (Figs. 7(B) and 8(B)). Merely administrating ICIs did not lead to TAM polarization, as indicated by low iNOS expression in IHC results. Flow cytometry analysis was performed to quantify the immune cells within tumors. The results for GL261 (Fig. 7(C–E)) showed slightly higher proportions of T cells ($CD3^+$ cells), cytotoxic T cells ($CD3^+CD8^+$ cells), and M1 macrophages ($F4/80^+iNOS^+$ cells) in aPD-L1/EV + aCTLA-4/EV-treated mice compared to the other treatment groups. On the other hand, ALTS1c1 tumors showed significantly more infiltrated T cells and polarized M1 macrophages with aPD-L1/EV + aCTLA-4/EV treatment compared to control and aPD-L1 + aCTLA-4 groups, both of which demonstrated similar proportions of immune cells within tumors (Fig. 8(C–E)). The gating strategy and antibody panel are listed in Fig. S13 and Table S2.

Several factors, including the cellular communications and cytokines interactions, have been suggested to play a role in establishing the tumor microenvironment (TME). The TME of different tumors consist distinct cellular components, leading to their different extent of reaction toward immunotherapy. Based on the lymphocytes infiltration density into the TME, the tumors can be classified as hot or cold tumors, and hot tumors were generally deemed to be more immune-active and more susceptible to immunotherapy [57]. The challenge in managing glioma with immunotherapeutic strategy lies in the fact that its TME remains immunosuppressive, and TAM, accounting for around 30 % of the tumor mass, contribute to the exhaustion of immune cells and lead to the poor response rate of gliomas toward immunotherapy [58,59]. To overcome the immunosuppressive TME, several strategies can be applied to transform the cold tumors into the hot ones, thus leading to the enhanced infiltration of cytotoxic lymphocytes to fight against tumor cells. Studies have suggested that polarizing TAM into the M1 phenotype overcomes the immunosuppressive condition and enhances immunotherapeutic efficacy [20,34,60]. A combination of immunotherapeutic strategies, including the blockade of multiple immune checkpoints with different mechanisms, can also be beneficial in activating immune responses within the TME [61]. In this study, EVs demonstrated an optimal TAM-polarizing effect toward the M1 phenotype (Fig. 3(C, D), 7 (B, E), 8(B, E)). The increased infiltration of T cells and cytotoxic T cells could be attributed to the M1 phenotype polarization of TAM that reversed the immunosuppressive TME and the efficient delivery of ICIs into the tumors with the aid of EVs, both of which realized the combination immunotherapy within the tumor. As observed in Figs. 5–8, the combination of EVs and ICIs treatment activated immune responses in the TME, leading to the downstream enhancement of immune effector cell infiltration and thus resulting in the optimal therapeutic effect [22, 62]. Based on the GL261 tumor volume results in Fig. 5 (C), it can be postulated that the combined immunotherapeutic effect can be achieved within ten days post treatment, resulting in the decreased tumor volume along with the prolonged survival duration.

The treatment outcomes of ICI/EVs were compared in two different orthotopic glioma mouse models due to the heterogenicity of the brain tumors [63]. The distinct cellular nature of GL261 (glioblastoma) and ALTS1c1 (astrocytoma) created different TME, and thus they reacted

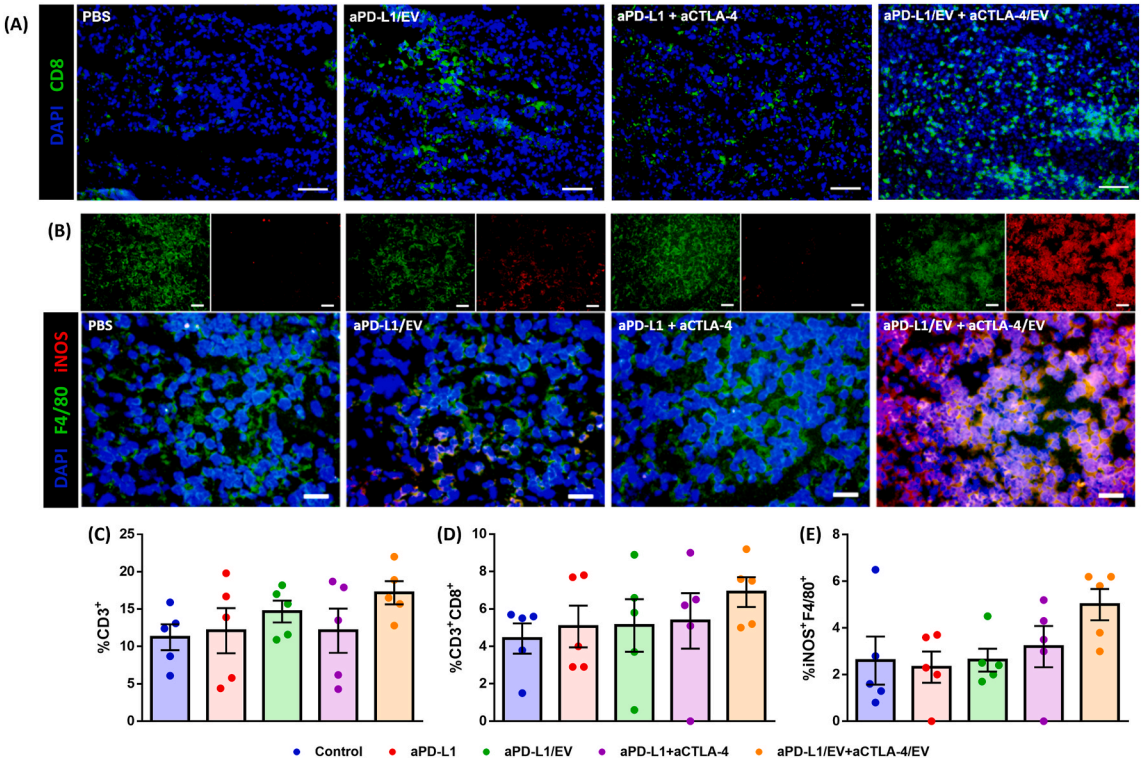


**Fig. 7.** Immune cells in GL261 tumors post treatment. (**A**) IHC images of cytotoxic T cells within the tumor tissue. Green fluorescence indicates CD8 expression on T cells, while nuclei are counterstained with DAPI. Scale bar: 50 μm. (**B**) IHC images of M1 macrophages within tumor tissue. Green fluorescence indicates F4/80-stained macrophages, and red fluorescence indicates iNOS expression. Nuclei are counterstained with DAPI. Scale bar: 20 μm. (**C-E**) Flow cytometry analysis results for total T cells (**C**), cytotoxic T cells (**D**), and M1 macrophages (**E**). Statistics for (**C, D, E**) were obtained from one-way ANOVA with Bonferroni post hoc test, with significance defined as $p < 0.05$. Data are expressed as mean ± SEM with n = 5.

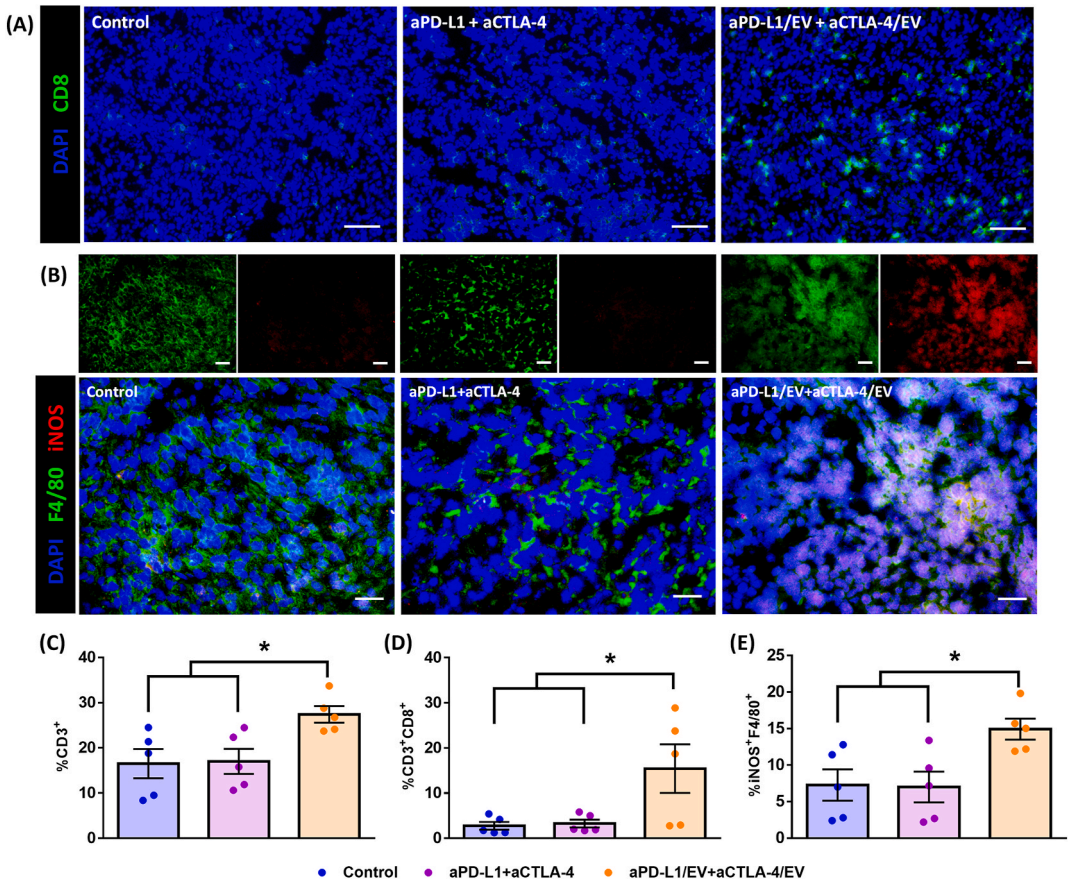


**Fig. 8.** Immune cells in ALTS1c1 tumors post treatment. (**A**) IHC images of cytotoxic T cells in tumor tissue. Green fluorescence indicated CD8 on T cells, and nuclei were counterstained with DAPI. Scale bar: 50 μm. (**B**) IHC images of M1 macrophages in tumor tissue. Green fluorescence indicated F4/80-stained macrophages and red fluorescence indicated iNOS expression. Nuclei were counterstained with DAPI. Scale bar: 20 μm. (**C-E**) Flow cytometry analysis results of total T cells (**C**), cytotoxic T cells (**D**), and M1 macrophages (**E**). Asterisks indicated significant difference compared to the other groups with statistics obtained from one-way ANOVA and Bonferroni post hoc test. Data were expressed as mean ± SEM with n = 5.

differently to ICI/EVs treatment (Fig. S14) [64,65]. The significant infiltration of cytotoxic T cells and TAM polarization in the IHC images of GL261 tumors upon ICI/EVs treatment could be the primary reason for the reduced tumor volume and prolonged survival duration (Fig. 5 (B–D)). The small tumor volume post aPD-L1/EV + aCTLA-4/EV treatment made it challenging to isolate tumor tissue for flow cytometry analysis. Nevertheless, the quantification results still demonstrated an increased presence of immune cells within GL261 tumors upon aPD-L1/EV + aCTLA-4/EV treatment. On the other hand, although a significant difference in T cell and M1 macrophage quantities was observed in ALTS1c1 tumors upon aPD-L1/EV + aCTLA-4/EV treatment (Fig. 8), the rapid growth of tumor cells [65] might be the reason for the slight prolongation of survival duration compared to the aPD-L1 + aCTLA-4 and control groups (Fig. 6). Given that EVs efficiently delivered ICIs into tumors, dose adjustment may be required to achieve an optimal therapeutic effect in ALTS1c1 tumors [66].

## 4. Conclusion

Numerous studies have focused on developing therapeutic strategies to manage glioma, and immunotherapy offers room for progress in achieving efficient glioma therapy. An ICIs delivery strategy with EVs was established in this study. A method to increase the secretion of proinflammatory EVs was developed, which is beneficial for drug delivery system preparation, and efficiently loaded with ICIs. A delivery strategy was established for the efficient accumulation of ICI/EVs within glioma lesion, activating the immune response and ultimately leading to the efficient management of glioma in mouse models. The results of this study suggest the feasibility of using CaP to obtain EVs for delivering ICIs. The simultaneous efficient delivery of ICIs and EVs modulates TME to exert an optimal therapeutic effect in glioma. In conclusion, the EVs-based drug delivery system established in this study holds promise for broad therapeutic applications in managing various brain diseases.

## CRediT authorship contribution statement

**Shang-Wen Lin:** Writing – original draft, Visualization, Validation, Methodology, Investigation, Formal analysis, Conceptualization. **Cheng-Ping Yu:** Validation, Methodology, Investigation, Formal analysis. **Jui-Chen Tsai:** Writing – review & editing, Supervision, Conceptualization. **Yan-Jye Shyong:** Writing – review & editing, Project administration, Funding acquisition, Conceptualization.

## Declaration of competing interest

The authors declare the following financial interests/personal relationships which may be considered as potential competing interests: Yan-Jye Shyong reports financial support was provided by National Science and Technology Council. If there are other authors, they declare that they have no known competing financial interests or personal relationships that could have appeared to influence the work reported in this paper.

## Data availability

Data will be made available on request.

## Acknowledgement

The authors thank Ping-Hsuan Wu in Dr. Teng-Hao Chen's lab in School of Pharmacy of National Cheng Kung University in facilitating the FTIR and XRD measurement of CaP. We also thank Professor Chi-Shiun Chiang in National Tsing-Hua University in providing us the ALTS1c1 cell line and taught us the method for establishing orthotopic glioma mouse model. The authors are grateful for the technical and animal experiment supports from the Core Research Laboratory and Laboratory Animal Center in College of Medicine, National Cheng Kung University, Tainan, Taiwan. We also acknowledge the use of TEM belonging to the Core Facility Center of the National Cheng Kung University. The authors are also grateful for the technical support for flow cytometry service from Taqkey Science Co., Ltd. This work is supported by National Science and Technology Council, Taiwan (NSTC 109-2628-E-006-001-MY3), and National Health Research Institutes, Taiwan (NHRI-EX111-11113EC) awarded to Yan-Jye Shyong.

## Appendix A. Supplementary data

Supplementary data to this article can be found online at https://doi.org/10.1016/j.mtbio.2024.101244.

## References

[1] P.Y. Wen, J.T. Huse, World health organization classification of central nervous system tumors, continuum (Minneap Minn) 23(6, Neuro Oncol. 2017 (2016) 1531–1547.
[2] A. Shergalis, A. Bankhead 3rd, U. Luesakul, N. Muangsin, N. Neamati, Current challenges and opportunities in treating glioblastoma, Pharmacol. Rev. 70 (3) (2018) 412–445.
[3] F. Hanif, K. Muzaffar, K. Perveen, S.M. Malhi, S.U. Simjee, Glioblastoma multiforme: a review of its epidemiology and pathogenesis through clinical presentation and treatment, Asian Pac J Cancer Prev 18 (1) (2017) 3–9.
[4] S. DiGrande, Is immunotherapy the future of glioblastoma treatment? Am. J. Manag. Care: Evid. base Oncol. 25 (2) (2019).
[5] C.-P. Yu, S.-W. Lin, J.-C. Tsai, Y.-J. Shyong, Long acting tariquidar loaded stearic acid-modified hydroxyapatite enhances brain penetration and antitumor effect of temozolomide, Eur. J. Pharm. Biopharm. 197 (2024) 114231.
[6] X. Wang, X. Hao, Y. Zhang, Q. Wu, J. Zhou, Z. Cheng, J. Chen, S. Liu, J. Pan, Y. Wang, J.-B. Fan, Bioinspired adaptive microdrugs enhance the chemotherapy of malignant glioma: beyond their nanodrugs, Adv. Mater. 36 (32) (2024) 2405165.
[7] M.F.M. Vismara, A. Donato, N. Malara, I. Presta, G. Donato, Immunotherapy in gliomas: are we reckoning without the innate immunity? International journal of immunopathology and pharmacology 33 (2019) 2058738419843378.
[8] J.A. Marin-Acevedo, E.O. Kimbrough, Y. Lou, Next generation of immune checkpoint inhibitors and beyond, J. Hematol. Oncol. 14 (1) (2021) 45.
[9] A. Galstyan, J.L. Markman, E.S. Shatalova, A. Chiechi, A.J. Korman, R. Patil, D. Klymyshyn, W.G. Tourtellotte, L.L. Israel, O. Braubach, V.A. Ljubimov, L. A. Mashouf, A. Ramesh, Z.B. Grodzinski, M.L. Penichet, K.L. Black, E. Holler, T. Sun, H. Ding, A.V. Ljubimov, J.Y. Ljubimova, Blood-brain barrier permeable nano immunoconjugates induce local immune responses for glioma therapy, Nat. Commun. 10 (1) (2019) 3850.
[10] D.A. Reardon, P.C. Gokhale, S.R. Klein, K.L. Ligon, S.J. Rodig, S.H. Ramkissoon, K. L. Jones, A.S. Conway, X. Liao, J. Zhou, P.Y. Wen, A.D. Van Den Abbeele, F.S. Hodi, L. Qin, N.E. Kohl, A.H. Sharpe, G. Dranoff, G.J. Freeman, Glioblastoma eradication following immune checkpoint blockade in an orthotopic, immunocompetent model, Cancer Immunol. Res. 4 (2) (2016) 124.
[11] A. Omuro, A.A. Brandes, A.F. Carpentier, A. Idbaih, D.A. Reardon, T. Cloughesy, A. Sumrall, J. Baehring, M. van den Bent, O. Bähr, G. Lombardi, P. Mulholland, G. Tabatabai, U. Lassen, J.M. Sepulveda, M. Khasraw, E. Vauleon, Y. Muragaki, A. M. Di Giacomo, N. Butowski, P. Roth, X. Qian, A.Z. Fu, Y. Liu, V. Potter, A. G. Chalamandaris, K. Tatsuoka, M. Lim, M. Weller, Radiotherapy combined with nivolumab or temozolomide for newly diagnosed glioblastoma with unmethylated MGMT promoter: an international randomized phase III trial, Neuro Oncol. 25 (1) (2023) 123–134.
[12] M. Lim, M. Weller, A. Idbaih, J. Steinbach, G. Finocchiaro, R.R. Raval, G. Ansstas, J. Baehring, J.W. Taylor, J. Honnorat, K. Petrecca, F. De Vos, A. Wick, A. Sumrall, S. Sahebjam, I.K. Mellinghoff, M. Kinoshita, M. Roberts, R. Slepetis, D. Warad, D. Leung, M. Lee, D.A. Reardon, A. Omuro, Phase III trial of chemoradiotherapy with temozolomide plus nivolumab or placebo for newly diagnosed glioblastoma with methylated MGMT promoter, Neuro Oncol. 24 (11) (2022) 1935–1949.
[13] L. Nayak, N. Standifer, J. Dietrich, J.L. Clarke, G.P. Dunn, M. Lim, T. Cloughesy, H. K. Gan, E. Flagg, E. George, S. Gaffey, J. Hayden, C. Holcroft, P.Y. Wen, M. Macri, A.J. Park, T. Ricciardi, A. Ryan, P. Schwarzenberger, R. Venhaus, M.L. Reyes, N. M. Durham, T. Creasy, R.Y. Huang, T. Kaley, D.A. Reardon, Circulating immune cell and outcome analysis from the phase II study of PD-L1 blockade with durvalumab for newly diagnosed and recurrent glioblastoma, Clin. Cancer Res. 28 (12) (2022) 2567–2578.
[14] T.-T. Tang, L.-L. Lv, H.-Y. Lan, B.-C. Liu, Extracellular vesicles: opportunities and challenges for the treatment of renal diseases, Front. Physiol. 10 (226) (2019).
[15] O.G. de Jong, S.A.A. Kooijmans, D.E. Murphy, L. Jiang, M.J.W. Evers, J.P. G. Sluijter, P. Vader, R.M. Schiffelers, Drug delivery with extracellular vesicles: from imagination to innovation, Accounts of chemical research 52 (7) (2019) 1761–1770.
[16] E.V. Batrakova, M.S. Kim, Using exosomes, naturally-equipped nanocarriers, for drug delivery, J. Contr. Release 219 (2015) 396–405.
[17] J. Chen, J. Pan, S. Liu, Y. Zhang, S. Sha, H. Guo, X. Wang, X. Hao, H. Zhou, S. Tao, Y. Wang, J.-B. Fan, Fruit-derived extracellular-vesicle-engineered structural droplet drugs for enhanced glioblastoma chemotherapy, Adv. Mater. 35 (45) (2023) 2304187.
[18] Y. Wang, M. Zhao, S. Liu, J. Guo, Y. Lu, J. Cheng, J. Liu, Macrophage-derived extracellular vesicles: diverse mediators of pathology and therapeutics in multiple diseases, Cell Death Dis. 11 (10) (2020) 924.
[19] H. Kim, S.Y. Wang, G. Kwak, Y. Yang, I.C. Kwon, S.H. Kim, Exosome-guided phenotypic switch of M1 to M2 macrophages for cutaneous wound healing, Adv. Sci. 6 (20) (2019) 1900513.
[20] X. Wang, H. Ding, Z. Li, Y. Peng, H. Tan, C. Wang, G. Huang, W. Li, G. Ma, W. Wei, Exploration and functionalization of M1-macrophage extracellular vesicles for effective accumulation in glioblastoma and strong synergistic therapeutic effects, Signal Transduct. Targeted Ther. 7 (1) (2022) 74.
[21] H. Jiang, L. Zhou, N. Shen, X. Ning, D. Wu, K. Jiang, X. Huang, M1 macrophage-derived exosomes and their key molecule lncRNA HOTTIP suppress head and neck squamous cell carcinoma progression by upregulating the TLR5/NF-κB pathway, Cell Death Dis. 13 (2) (2022) 183.
[22] L. Cheng, Y. Wang, L. Huang, Exosomes from M1-polarized macrophages potentiate the cancer vaccine by creating a pro-inflammatory microenvironment in the lymph node, Mol. Ther. 25 (7) (2017) 1665–1675.
[23] A. Savina, M. Furlán, M. Vidal, M.I. Colombo, Exosome release is regulated by a calcium-dependent mechanism in K562 cells, J. Biol. Chem. 278 (22) (2003) 20083–20090.
[24] J. Taylor, I. Azimi, G. Monteith, M. Bebawy, Ca2+ mediates extracellular vesicle biogenesis through alternate pathways in malignancy, J. Extracell. Vesicles 9 (1) (2020) 1734326.
[25] S.W. Messenger, S.S. Woo, Z. Sun, T.F.J. Martin, A Ca2+-stimulated exosome release pathway in cancer cells is regulated by Munc13-4, The Journal of cell biology 217 (8) (2018) 2877–2890.
[26] F. Bakan, Gene delivery by hydroxyapatite and calcium phosphate nanoparticles: a review of novel and recent applications, in: J. Thirumalai (Ed.), Hydroxyapatite - Advances in Composite Nanomaterials, Biomedical Applications and its Technological Facets, IntechOpen, 2017.
[27] M. Parent, H. Baradari, E. Champion, C. Damia, M. Viana-Trecant, Design of calcium phosphate ceramics for drug delivery applications in bone diseases: a review of the parameters affecting the loading and release of the therapeutic substance, J. Contr. Release 252 (2017) 1–17.
[28] Y. Dautova, A.N. Kapustin, K. Pappert, M. Epple, H. Okkenhaug, S.J. Cook, C. M. Shanahan, M.D. Bootman, D. Proudfoot, Calcium phosphate particles stimulate interleukin-1β release from human vascular smooth muscle cells: a role for spleen tyrosine kinase and exosome release, J. Mol. Cell. Cardiol. 115 (2018) 82–93.
[29] Q. Liu, Y. Luo, Y. Zhao, P. Xiang, J. Zhu, W. Jing, W. Jin, M. Chen, R. Tang, H. Yu, Nano-hydroxyapatite accelerates vascular calcification via lysosome impairment and autophagy dysfunction in smooth muscle cells, Bioact. Mater. 8 (2022) 478–493.
[30] Y.-J. Shyong, K.-C. Chang, F.-H. Lin, Calcium phosphate particles stimulate exosome secretion from phagocytes for the enhancement of drug delivery, Colloids Surf. B Biointerfaces 171 (2018) 391–397.
[31] L. Alvarez-Erviti, Y. Seow, H. Yin, C. Betts, S. Lakhal, M.J. Wood, Delivery of siRNA to the mouse brain by systemic injection of targeted exosomes, Nat. Biotechnol. 29 (4) (2011) 341–345.
[32] Z. Yang, J. Shi, J. Xie, Y. Wang, J. Sun, T. Liu, Y. Zhao, X. Zhao, X. Wang, Y. Ma, V. Malkoc, C. Chiang, W. Deng, Y. Chen, Y. Fu, K.J. Kwak, Y. Fan, C. Kang, C. Yin, J. Rhee, P. Bertani, J. Otero, W. Lu, K. Yun, A.S. Lee, W. Jiang, L. Teng, B.Y.S. Kim, L.J. Lee, Large-scale generation of functional mRNA-encapsulating exosomes via cellular nanoporation, Nat. Biomed. Eng. 4 (1) (2020) 69–83.
[33] M.J. Haney, N.L. Klyachko, Y. Zhao, R. Gupta, E.G. Plotnikova, Z. He, T. Patel, A. Piroyan, M. Sokolsky, A.V. Kabanov, E.V. Batrakova, Exosomes as drug delivery vehicles for Parkinson's disease therapy, J. Contr. Release 207 (2015) 18–30.
[34] Y.W. Choo, M. Kang, H.Y. Kim, J. Han, S. Kang, J.-R. Lee, G.-J. Jeong, S.P. Kwon, S. Y. Song, S. Go, M. Jung, J. Hong, B.-S. Kim, M1 macrophage-derived nanovesicles potentiate the anticancer efficacy of immune checkpoint inhibitors, ACS Nano 12 (9) (2018) 8977–8993.
[35] C. Théry, K.W. Witwer, E. Aikawa, M.J. Alcaraz, J.D. Anderson, R. Andriantsitohaina, A. Antoniou, T. Arab, F. Archer, G.K. Atkin-Smith, D.C. Ayre, J.-M. Bach, D. Bachurski, H. Baharvand, L. Balaj, S. Baldacchino, N.N. Bauer, A. A. Baxter, M. Bebawy, C. Beckham, A. Bedina Zavec, A. Benmoussa, A.C. Berardi, P. Bergese, E. Bielska, C. Blenkiron, S. Bobis-Wozowicz, E. Boilard, W. Boireau, A. Bongiovanni, F.E. Borràs, S. Bosch, C.M. Boulanger, X. Breakefield, A.M. Breglio, M.Á. Brennan, D.R. Brigstock, A. Brisson, M.L. Broekman, J.F. Bromberg, P. Bryl-Górecka, S. Buch, A.H. Buck, D. Burger, S. Busatto, D. Buschmann, B. Bussolati, E. I. Buzás, J.B. Byrd, G. Camussi, D.R. Carter, S. Caruso, L.W. Chamley, Y.-T. Chang, C. Chen, S. Chen, L. Cheng, A.R. Chin, A. Clayton, S.P. Clerici, A. Cocks, E. Cocucci, R.J. Coffey, A. Cordeiro-da-Silva, Y. Couch, F.A. Coumans, B. Coyle, R. Crescitelli, M.F. Criado, C. D'Souza-Schorey, S. Das, A. Datta Chaudhuri, P. de Candia, E.F. De

Santana, O. De Wever, H.A. Del Portillo, T. Demaret, S. Deville, A. Devitt, B. Dhondt, D. Di Vizio, L.C. Dieterich, V. Dolo, A.P. Dominguez Rubio, M. Dominici, M.R. Dourado, T.A. Driedonks, F.V. Duarte, H.M. Duncan, R. M. Eichenberger, K. Ekström, S. El Andaloussi, C. Elie-Caille, U. Erdbrügger, J. M. Falcón-Pérez, F. Fatima, J.E. Fish, M. Flores-Bellver, A. Försönits, A. Frelet-Barrand, F. Fricke, G. Fuhrmann, S. Gabrielsson, A. Gámez-Valero, C. Gardiner, K. Gärtner, R. Gaudin, Y.S. Gho, B. Giebel, C. Gilbert, M. Gimona, I. Giusti, D. C. Goberdhan, A. Görgens, S.M. Gorski, D.W. Greening, J.C. Gross, A. Gualerzi, G. N. Gupta, D. Gustafson, A. Handberg, R.A. Haraszti, P. Harrison, H. Hegyesi, A. Hendrix, A.F. Hill, F.H. Hochberg, K.F. Hoffmann, B. Holder, H. Holthofer, B. Hosseinkhani, G. Hu, Y. Huang, V. Huber, S. Hunt, A.G.-E. Ibrahim, T. Ikezu, J. M. Inal, M. Isin, A. Ivanova, H.K. Jackson, S. Jacobsen, S.M. Jay, M. Jayachandran, G. Jenster, L. Jiang, S.M. Johnson, J.C. Jones, A. Jong, T. Jovanovic-Talisman, S. Jung, R. Kalluri, S.-I. Kano, S. Kaur, Y. Kawamura, E.T. Keller, D. Khamari, E. Khomyakova, A. Khvorova, P. Kierulf, K.P. Kim, T. Kislinger, M. Klingeborn, D. J. Klinke 2nd, M. Kornek, M.M. Kosanović, Á.F. Kovács, E.-M. Krämer-Albers, S. Krasemann, M. Krause, I.V. Kurochkin, G.D. Kusuma, S. Kuypers, S. Laitinen, S. M. Langevin, L.R. Languino, J. Lannigan, C. Lässer, L.C. Laurent, G. Lavieu, E. Lázaro-Ibáñez, S. Le Lay, M.-S. Lee, Y.X.F. Lee, D.S. Lemos, M. Lenassi, A. Leszczynska, I.T. Li, K. Liao, S.F. Libregts, E. Ligeti, R. Lim, S.K. Lim, A. Linē, K. Linnemannstöns, A. Llorente, C.A. Lombard, M.J. Lorenowicz, Á.M. Lörincz, J. Lötvall, J. Lovett, M.C. Lowry, X. Loyer, Q. Lu, B. Lukomska, T.R. Lunavat, S. L. Maas, H. Malhi, A. Marcilla, J. Mariani, J. Mariscal, E.S. Martens-Uzunova, L. Martin-Jaular, M.C. Martinez, V.R. Martins, M. Mathieu, S. Mathivanan, M. Maugeri, L.K. McGinnis, M.J. McVey, D.G. Meckes Jr., K.L. Meehan, I. Mertens, V.R. Minciacchi, A. Möller, M. Møller Jørgensen, A. Morales-Kastresana, J. Morhayim, F. Mullier, M. Muraca, L. Musante, V. Mussack, D.C. Muth, K. H. Myburgh, T. Najrana, M. Nawaz, I. Nazarenko, P. Nejsum, C. Neri, T. Neri, R. Nieuwland, L. Nimrichter, J.P. Nolan, E.N. Nolte-'t Hoen, N. Noren Hooten, L. O'Driscoll, T. O'Grady, A. O'Loghlen, T. Ochiya, M. Olivier, A. Ortiz, L.A. Ortiz, X. Osteikoetxea, O. Østergaard, M. Ostrowski, J. Park, D.M. Pegtel, H. Peinado, F. Perut, M.W. Pfaffl, D.G. Phinney, B.C. Pieters, R.C. Pink, D.S. Pisetsky, E. Pogge von Strandmann, I. Polakovicova, I.K. Poon, B.H. Powell, I. Prada, L. Pulliam, P. Quesenberry, A. Radeghieri, R.L. Raffai, S. Raimondo, J. Rak, M.I. Ramirez, G. Raposo, M.S. Rayyan, N. Regev-Rudzki, F.L. Ricklefs, P.D. Robbins, D. D. Roberts, S.C. Rodrigues, E. Rohde, S. Rome, K.M. Rouschop, A. Rughetti, A. E. Russell, P. Saá, S. Sahoo, E. Salas-Huenuleo, C. Sánchez, J.A. Saugstad, M. J. Saul, R.M. Schiffelers, R. Schneider, T.H. Schøyen, A. Scott, E. Shahaj, S. Sharma, O. Shatnyeva, F. Shekari, G.V. Shelke, A.K. Shetty, K. Shiba, P.R.M. Siljander, A. M. Silva, A. Skowronek, O.L. Snyder 2nd, R.P. Soares, B.W. Sódar, C. Soekmadji, J. Sotillo, P.D. Stahl, W. Stoorvogel, S.L. Stott, E.F. Strasser, S. Swift, H. Tahara, M. Tewari, K. Timms, S. Tiwari, R. Tixeira, M. Tkach, W.S. Toh, R. Tomasini, A. C. Torrecilhas, J.P. Tosar, V. Toxavidis, L. Urbanelli, P. Vader, B.W. van Balkom, S. G. van der Grein, J. Van Deun, M.J. van Herwijnen, K. Van Keuren-Jensen, G. van Niel, M.E. van Royen, A.J. van Wijnen, M.H. Vasconcelos, I.J. Vechetti Jr., T. D. Veit, L.J. Vella, É. Velot, F.J. Verweij, B. Vestad, J.L. Viñas, T. Visnovitz, K. V. Vukman, J. Wahlgren, D.C. Watson, M.H. Wauben, A. Weaver, J.P. Webber, V. Weber, A.M. Wehman, D.J. Weiss, J.A. Welsh, S. Wendt, A.M. Wheelock, Z. Wiener, L. Witte, J. Wolfram, A. Xagorari, P. Xander, J. Xu, X. Yan, M. Yáñez-Mó, H. Yin, Y. Yuana, V. Zappulli, J. Zarubova, V. Žėkas, J.-Y. Zhang, Z. Zhao, L. Zheng, A.R. Zheutlin, A.M. Zickler, P. Zimmermann, A.M. Zivkovic, D. Zocco, E. K. Zuba-Surma, Minimal information for studies of extracellular vesicles 2018 (MISEV2018): a position statement of the International Society for Extracellular Vesicles and update of the MISEV2014 guidelines, J. Extracell. Vesicles 7 (1) (2018) 1535750, 1535750.

[36] S. Zalba, A.M. Contreras-Sandoval, E. Martisova, R. Debets, C. Smerdou, M. J. Garrido, Quantification of pharmacokinetic profiles of PD-1/PD-L1 antibodies by validated ELISAs, Pharmaceutics 12 (6) (2020) 595.

[37] M.G. Ma, Hierarchically nanostructured hydroxyapatite: hydrothermal synthesis, morphology control, growth mechanism, and biological activity, Int. J. Nanomed. 7 (2012) 1781–1791.

[38] B.X. Vuong, Synthesis and characterization of HA/β-TCP bioceramic powder, Vietnam Journal of Chemistry 56 (2) (2018) 152–155.

[39] Z. Liu, Y. Xiao, W. Chen, Y. Wang, B. Wang, G. Wang, X. Xu, R. Tang, Calcium phosphate nanoparticles primarily induce cell necrosis through lysosomal rupture: the origination of material cytotoxicity, J. Mater. Chem. B 2 (22) (2014) 3480–3489.

[40] P. Berraondo, M.F. Sanmamed, M.C. Ochoa, I. Etxeberria, M.A. Aznar, J.L. Pérez-Gracia, M.E. Rodríguez-Ruiz, M. Ponz-Sarvise, E. Castañón, I. Melero, Cytokines in clinical cancer immunotherapy, Br. J. Cancer 120 (1) (2019) 6–15.

[41] B. Pazár, H.-K. Ea, S. Narayan, L. Kolly, N. Bagnoud, V. Chobaz, T. Roger, F. Lioté, A. So, N. Busso, Basic calcium phosphate crystals induce monocyte/macrophage IL-1β secretion through the NLRP3 inflammasome in vitro, J. Immunol. 186 (4) (2011) 2495.

[42] E. Uribe-Querol, C. Rosales, Phagocytosis: our current understanding of a universal biological process, Front. Immunol. 11 (2020).

[43] J.A. Champion, A. Walker, S. Mitragotri, Role of particle size in phagocytosis of polymeric microspheres, Pharmaceut. Res. 25 (8) (2008) 1815–1821.

[44] S.K. Frandsen, M. Vissing, J. Gehl, A comprehensive review of calcium electroporation -A novel cancer treatment modality, Cancers 12 (2) (2020).

[45] A.C. Wyse-Jackson, S.L. Roche, A.M. Ruiz-Lopez, J.N. Moloney, A.M. Byrne, T. G. Cotter, Progesterone analogue protects stressed photoreceptors via bFGF-mediated calcium influx, Eur. J. Neurosci. 44 (12) (2016) 3067–3079.

[46] C. Sánchez-Cárdenas, A. Romarowski, G. Orta, J.L. De la Vega-Beltrán, D. Martín-Hidalgo, A. Hernández-Cruz, P.E. Visconti, A. Darszon, Starvation induces an increase in intracellular calcium and potentiates the progesterone-induced mouse sperm acrosome reaction, Faseb. J. : official publication of the Federation of American Societies for Experimental Biology 35 (4) (2021) e21528.

[47] F. Püschel, F. Favaro, J. Redondo-Pedraza, E. Lucendo, R. Iurlaro, S. Marchetti, B. Majem, E. Eldering, E. Nadal, J.E. Ricci, E. Chevet, C. Muñoz-Pinedo, Starvation and antimetabolic therapy promote cytokine release and recruitment of immune cells, Proc. Natl. Acad. Sci. U.S.A. 117 (18) (2020) 9932–9941.

[48] G. Arango Duque, A. Descoteaux, Macrophage cytokines: involvement in immunity and infectious diseases, Front. Immunol. 5 (2014) 491, 491.

[49] M. Dash, K. Palaniyandi, S. Ramalingam, S. Sahabudeen, N.S. Raja, Exosomes isolated from two different cell lines using three different isolation techniques show variation in physical and molecular characteristics, Biochim. Biophys. Acta Biomembr. 1863 (2) (2021) 183490.

[50] S.-W. Lin, Y.-J. Shyong, P.-C. Kuo, J.-C. Tsai, Topical application of sebacoyl dinalbuphine ester-loaded nanostructured lipid carriers alleviate pruritus in scratching mouse model, Int. J. Pharm. 600 (2021) 120400.

[51] S.-W. Lin, J.-C. Tsai, Y.-J. Shyong, Drug delivery of extracellular vesicles: preparation, delivery strategies and applications, Int. J. Pharm. 642 (2023) 123185.

[52] A. Haasbroek-Pheiffer, S. Van Niekerk, F. Van der Kooy, T. Cloete, J. Steenekamp, J. Hamman, In vitro and ex vivo experimental models for evaluation of intranasal systemic drug delivery as well as direct nose-to-brain drug delivery, Biopharm Drug Dispos. 44 (1) (2023) 94–112.

[53] M. Jerebtsova, X. Ye, P.E. Ray, A simple technique to establish a long-term adenovirus mediated gene transfer to the heart of newborn mice, Cardiovascular & hematological disorders drug targets 9 (2) (2009) 136–140.

[54] N.N. Kumar, J.J. Lochhead, M.E. Pizzo, G. Nehra, S. Boroumand, G. Greene, R. G. Thorne, Delivery of immunoglobulin G antibodies to the rat nervous system following intranasal administration: distribution, dose-response, and mechanisms of delivery, J. Contr. Release 286 (2018) 467–484.

[55] M. Wang, X. Zhai, J. Li, J. Guan, S. Xu, Y. Li, H. Zhu, The role of cytokines in predicting the response and adverse events related to immune checkpoint inhibitors, Front. Immunol. 12 (2021).

[56] X. Zhang, X. Lu, Y. Yu, K. Tan, H. Cui, Changes of IL-6 and IFN-γ before and after the adverse events related to immune checkpoint inhibitors: a retrospective study, Medicine 101 (46) (2022) e31761.

[57] W. Yang, S. Liu, M. Mao, Y. Gong, X. Li, T. Lei, C. Liu, S. Wu, Q. Hu, T-cell infiltration and its regulatory mechanisms in cancers: insights at single-cell resolution, J. Exp. Clin. Cancer Res. 43 (1) (2024) 38.

[58] D.F. Quail, J.A. Joyce, The microenvironmental landscape of brain tumors, Cancer Cell 31 (3) (2017) 326–341.

[59] A.F. Haddad, J.S. Young, S. Gill, M.K. Aghi, Resistance to immune checkpoint blockade: mechanisms, counter-acting approaches, and future directions, Semin. Cancer Biol. 86 (Pt 3) (2022) 532–541.

[60] D. Saha, R.L. Martuza, S.D. Rabkin, Macrophage polarization contributes to glioblastoma eradication by combination immunovirotherapy and immune checkpoint blockade, Cancer Cell 32 (2) (2017) 253–267.e5.

[61] M. Bausart, V. Préat, A. Malfanti, Immunotherapy for glioblastoma: the promise of combination strategies, J. Exp. Clin. Cancer Res. 41 (1) (2022) 35.

[62] G.R. Gunassekaran, S.M. Poongkavithai Vadevoo, M.-C. Baek, B. Lee, M1 macrophage exosomes engineered to foster M1 polarization and target the IL-4 receptor inhibit tumor growth by reprogramming tumor-associated macrophages into M1-like macrophages, Biomaterials 278 (2021) 121137.

[63] D.N. Louis, A. Perry, P. Wesseling, D.J. Brat, I.A. Cree, D. Figarella-Branger, C. Hawkins, H.K. Ng, S.M. Pfister, G. Reifenberger, R. Soffietti, A. von Deimling, D. W. Ellison, The 2021 WHO classification of tumors of the central nervous system: a summary, Neuro Oncol. 23 (8) (2021) 1231–1251.

[64] C.-M. Lin, C.-F. Yu, H.-Y. Huang, F.-H. Chen, J.-H. Hong, C.-S. Chiang, Distinct tumor microenvironment at tumor edge as a result of astrocyte activation is associated with therapeutic resistance for brain tumor, Front. Oncol. 9 (307) (2019).

[65] S.-C. Wang, J.-H. Hong, C. Hsueh, C.-S. Chiang, Tumor-secreted SDF-1 promotes glioma invasiveness and TAM tropism toward hypoxia in a murine astrocytoma model, Lab. Invest. 92 (1) (2012) 151–162.

[66] S.-W. Lin, Delivery of Immune Checkpoint Inhibitors with Extracellular Vesicles in the Management of Glioma, Institute of Clinical Pharmacy and Pharmaceutical Sciences, National Cheng Kung University, Theses and Dissertations of National Cheng Kung University, 2023, p. 92.